1-26-2016 12:00 AM

The Study of Nano-optics In Hybrid Systems

Marek J. Brzozowski
The University of Western Ontario

Supervisor
Mahi R. Singh
The University of Western Ontario

Graduate Program in Physics
A thesis submitted in partial fulfillment of the requirements for the degree in Master of Science

Abstract

In this thesis, we study the quantum light-matter interaction in polaritonic heterostructures. These systems are made by combining various nanocomponents, such as quantum dots, graphene films, metallic nanoparticles and metamaterials. These heterostructures are used to develop new optoelectronic devices due to the interaction between nanocomposites.

Photoluminescence quenching and absorption spectrum are determined and an explanatory theory is developed for these polaritonic heterostructures. Photoluminescence quenching is evaluated for a graphene, metallic nanoparticle and quantum dot system. It is shown that average distance between nanocomposites or concentration of nanocomposites affect the output these system produced. Photoluminescence quenching was also evaluated for a metamaterial hybrid system.

Lastly, the absorption spectrum of quantum dots was calculated in a quantum dot and metamaterial system. The metamaterial contained two surface plasmon modes which if in resonance with excitons of the quantum dot shown an enhancement in the absorption spectrum of the quantum dot.

Keywords: Plasmonics, surface plasmon polaritons, excitons, nanocomposites, graphene, metamaterials, quantum dots, metallic nanoparticles, density matrix method

Co-Authorship Statement

This thesis contains both material communicated with publishers and unpublished, soon to be communicated results.

For the material presented in chapters 3,4, and 5 Marek Brzozowski and Mahi Singh developed the theoretical formalism and wrote the manuscript. Marek Brzozowski performed the numerical calculations and produced the results with consultation with Mahi Singh

For my family.

Acknowledgement

I would like to express my foremost appreciation to my supervisor, Professor Mahi Singh, for his support and patience during the past two years. I have been fortunate to have supervisor with so much dedication to his students who was always available to answer problems. His vast knowledge of physics and work ethic were critical components in the completion of this thesis.

A large thank you goes to my graduate colleagues Shankar Balakrishnan, Kieffer Davieau, Chris Racknor, Joel Cox, and Ethan Pitambar. Without their support and friendship my graduate experience would be much more strenuous and not as engaging. Cheers.

For the very talented faculty, staff members, and the students of the Physics and Astronomy department at Western University, which has been my home for my undergraduate and graduate life, I would like to pass on my gratitute for their friendly support and wonderful care. Specifically, I would like to thank my advisory committee members Professors Eugene Wong and Margaret Campbell-Brown for their guidance.

Additionally, I would like to thank my mother, father, sister, and brother for their unconditional love and endless support, without them I would have not been so fortunate. To all my friends: Thank you for the countless adventures and wonderful memories. Lastly, a special gratitude and appreciation to my lovely partner, Amanda, for her immeasurable love, encouragement and kindness. Without her this would have not been possible.

Contents

Abstract i

Co-Authorship Statement ii

Dedication iii

Acknowledgement iv

List of Figures viii

List of Abbreviations xii

1 Fundamentals 1

1.1 Plasmonics 1

1.2 Surface Plasmon Polaritons 3

1.3 Photoluminescence 5

1.4 Graphene 6

1.5 Metamaterials 7

1.6 Quantum Emitters 8

1.7 Density Matrix Method 9

2 Introduction 12

2.1 Photoluminescence Quenching in Graphene Hybrid Nanosystems 12

2.2 Photoluminescence Quenching in Metamaterial Nanosystems 14

2.3 Plasmonics in Metamaterial Nanosystems 16
2.4 Objective and Outline of the Thesis 17

3 Photoluminescence quenching, metallic nanoparticle and graphene hybrid nanomaterials 25

3.1 Introduction 25
3.2 Theoretical Formalism 27
3.2.1 Photoluminescence 27
3.2.2 Density matrix method and photoluminescence 33
3.3 Results and Discussion 37
3.4 Conclusions 44

4 Photoluminescence quenching theory in metamaterial, quantum dots and metallic nanoparticles hybrid systems including local fields 49

4.1 Introduction 50
4.2 Theoretical Formalism 51
4.2.1 Photoluminescence quenching 51
4.2.2 System Fields Contribution of metallic nanoparticles and metamaterial . 53
4.2.3 Density Matrix Equation and Quenching Factor 56
4.3 Results and Discussions 58
4.4 Conclusions 62

5 Light absorbtion in quantum dots and nano-hole metamaterial structure 66

5.1 Introduction 66
5.2 Theoretical Formalism 68
5.2.1 Surface plasmon polaritons in nano-hole structure 68
5.2.2 Coupling of Quantum emitter and nano-hole structure 70
5.2.3 Exciton-SPP interactions 73
5.2.4 Absorption coefficient and Density matrix method 76

5.3 Results and Discussion 77
5.4 Conclusion 81

6 Concluding Remarks **85**

7 Future Work **87**

Curriculum Vitae **90**

List of Figures

1.1 Permittivity of metals following the Drude model. Horizontal intercept corresponds to the metal's plasmon frequency. 2

1.2 Schematic illustration of an surface plasmon polariton propagating along a metal-dielectric interface. These waves can be excited by an electromagnetic light with E=hv. 3

1.3 Dispersion relation of plasmon polaritons within a metal-dielectric system. The lower curve corresponds to the surface plasmon polaritons where the limit corresponds to the surface plasmon polariton frequency. The higher curve indicates the plasmon polaritons found in the bulk metal, and the lower limit of this curve indicates plasmon frequency of the metal. 4

1.4 Illustration of the photoluminescence process. An initial photon causes an excitation, after some time a photon is released due a decay from the excited state to the ground. 5

1.5 A.)Schematic representation of a 2D graphene lattice. Vertices correspond to individual carbon atom. b.) Dispersion relation of a 2d graphene lattice. The Dirac point is the overlapping point between graphene's conductions and valence band. The fermi level is above the Dirac point thus the carriers are electronic like [3]. 6

1.6 A metamaterial structure consisting of an array of metallic split ring resonators and metallic rod. Inset: An equivalent L-C electric circuit schematic of the unit cell. 7

1.7 Splitting energy levels in semiconductor quantum dots due to quantum energy levels. Band gaps decrease as quantum dots increase in size. 9

3.1 A schematic diagram of QD-MNP-GR hybrid system deposited on a liquid or solid material. 27

3.2 PL emission spectra of QE-GR system. The solid curves correspond to theoretical results, while the solid circular dots indicate experimental result. Curve and solid circles of A indicate QE without GR. Curves and solid circles of B-G indicate QE-GR hybrid system with GR concentrations of 0.02, 0.04, 0.06 0.08 0.10 0.012 $\mu g/mL$ and R_{QG} of 29, 22, 17, 13, 8, 6 nm. 38

3.3 Concentration (μg/mL) of GR plotted as a function of $R_{QG}(nm)$. The solid curve represents an exponential line of best fit. 40

3.4 PL emission spectra of QE-MNP-GR system. The solid curves correspond to theoretical results, while the solid circular dots indicate experimental result. Curve and solid circles of A indicate QE without GR and MNP. Curves and solid circles of B indicate QE-MNP hybrid system with R_{QM} = 10nm. Curves and solid circles of C indicate QE-MNP-GR hybrid system with R_{QM} = R_{QG} =10nm and R_{MG} = 20nm. Solid circles of C and D indicate QE-MNP-GR bound with antigen concentration of 0.1ng/mL and 0.05ng/mL, respectively. Curves of C and D represent QE-MNP-GR with R_{QM} = 40nm, R_{QG} =14nm and R_{QM} = 30nm R_{QG} =13nm and R_{MG} = 20nm, respectively. 41

3.5 Normalized decay rate (A.U.) is plotted as a function of $R_{MG}(nm)$. The solid line corresponds to the PL efficiency without indirect nonradiative term, while the dotted curve corresponds to the PL efficiency with the indirect nonradiative term. Here, R_{QM} = R_{QG} =10nm. 43

3.6 Plot of the Im ρ_{ba} as a function of normalized time, $\tau = \Gamma_N t/\hbar$. The solid curve represents when only Φ_{QMG} is present and the rest of the terms are absent, with $R_{QG} = 15nm$ and $R_{QM} = 10nm$.The dotted curve corresponds when only Φ_{QGM} is present and the rest of terms are absent, with $R_{QG} = 10nm$ and $R_{QM} = 15nm$.The other parameters are $R_{MG} = 10nm$, and $\hbar\omega$ =2.18eV. 44

4.1 a) A schematic diagram of SRM-MNP-QD hybrid system deposited on a dielectric substrate. b) A schematic diagram of a QD with three energy levels in a V-configuration. Level |a⟩ indicates the ground level while levels |b⟩ and |c⟩ corresponds to two excited states. Metamaterial's SPP couples with transition |a⟩ - |b⟩ of the QD while MNP's SPP couples with transition |a⟩ - |c⟩. 51

4.2 Quenching factor for a QD. Solid curve corresponds quenching without SRM-MNP, while the dashed curve corresponds to a system with SRM-MNP where all segments are 10nm apart. 58

4.3 PL emission spectra of a QD-MNP-SRM system. The dashed and dotted curve corresponds to distances of $R_{QM} = 15$ and $R_{QM} = 20$, respectively, while $R_{QS} = R_{SM} = 10nm$. 60

4.4 PL emission spectra of a QD-MNP-SRM system. The dashed and dotted curve corresponds to distances of $R_{QS} = 15nm$ and $R_{QS} = 20nm$, respectively, while $R_{QM} = R_{SM} = 10nm$. 61

4.5 PL emission spectra of a QD-MNP-SRM system. The dashed and dotted curve corresponds to distances of $R_{SM} = 15nm$ and $R_{SM} = 2nm0$, respectively, while $R_{QM} = R_{QS} = 10nm$. 62

5.1 a) A schematic diagram of NAS-QD hybrid system deposited on Pyrex. b) Unit cell of the NAS is illustrated. c) An electric schematic of the SRM unit cell, composed of capacitors and inductors. 68

5.2 Surface plasmon polariton dispersion relation of the nano-hole metamaterial structure. Solid curve corresponds to n=0 while the dashed curve represents n=1. Other parameters include a_p = 360nm and r = 50nm. 70

5.3 A schematic diagram of a QD with three energy levels in a V-configuration. Level |a⟩ indicates the ground level while levels |b⟩ and |c⟩ corresponds to two excited states. Metamaterial's SPP (when n=0) couples with transition |a⟩ - |b⟩ of the QD while metamaterial's SPP (when n=1) couples with transition |a⟩ - |c⟩. 73

5.4 Plot of the absorption coefficient of the QD as a function of energy for (a) when the SPP of the first mode (n=0) resonants with the QD and (b) when the SPP from the second mode (n=1) resonants with the QD. Solid curves correspond to the energies where both modes of SPPs are not resonant with the QD. 78

5.5 Plot of the absorption coefficient of the QD as a function of energy for when both modes of the SPPs resonant with the QD. The solid curve corresponds to when R, the center-to-center distance between components, is R = 15nm while the dashed curve corresponds to R= 13.5nm. 79

5.6 a) Plot of the normalized absorption coefficient (α/α_0) as a function of normalized time, $\tau = \gamma_b 2/2$. b) Plot of the population as a function of normalized time, $\tau = \gamma_b 2/2$. The dashed curves and solid curves correspond to when the system is in resonance and non-resonance, respectively. Other parameters include R=15nm, $\epsilon = 2.27eV$ 81

List of Abbreviations

DDI	Dipole-dipole Interaction
GR	Graphene
MNP	Metallic Nanoparticles
NAS	Nano-hole Array Structure
QD	Quantum Dot
QE	Quantum Emitter
PL	Photoluminescence
SPP	Surface Plasmon Polariton
SRM	Split-ring Metamaterial

Chapter 1

Fundamentals

In this thesis we study plasmonics; therefore, the fundamental concepts required to follow the thesis are introduced in this chapter. The objective of the chapter is to provide the reader with a short and casual introduction to the concepts, structures, and processes that will be further discussed in the thesis.

1.1 Plasmonics

Developing nanoscale optoelectronics based on heterostructure used for a variety of applications has been growing in interest. In developing these systems, the study of Plasmonics has played a crucial role. Plasmonics is the study of the interaction between free electrons in metallic like structures with electromagnetic fields. Free electrons in metals have random motion. An applied electric component from an electromagnetic field give these free electrons a collective oscillation. This collective oscillation is called a plasmon. Plasmons present in bulk materials are called bulk plasmons, while plasmons at the surface are classified as surface plasmons [1]. Most research is conducted on surface plasmon, due to the high lossy behavior in bulk plasmons present in noble metals [2].

Consider a conductor has n number of electrons per volume, each with the mass and a charge of m_e and e, respectively. An applied electromagnetic field $\mathbf{E} = E_0 \exp(i\omega t)$ with an

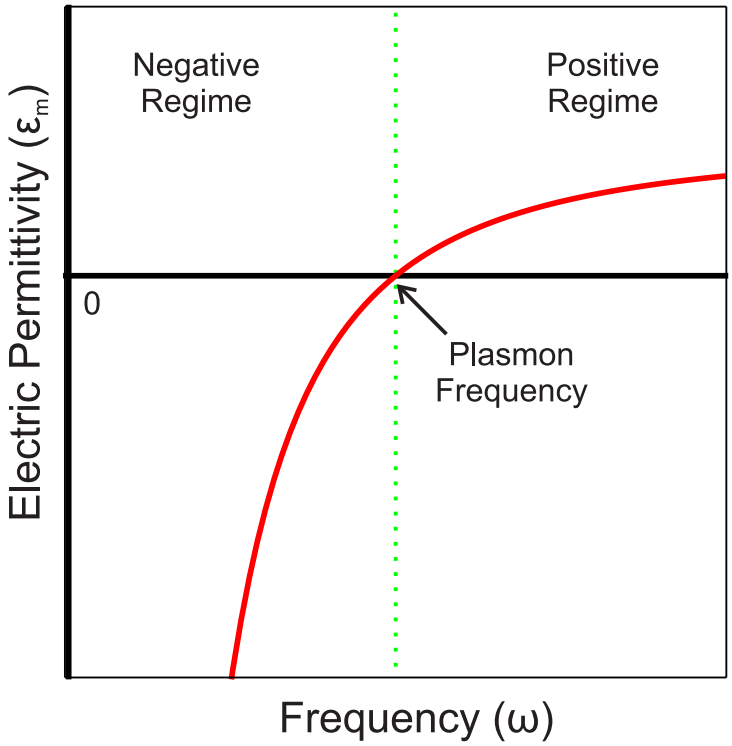

Figure 1.1: Permittivity of metals following the Drude model. Horizontal intercept corresponds to the metal's plasmon frequency.

amplitude E_0 and a frequency ω induces an oscillatory dipole moment to the conductor, due to the displacement of the electrons with respect to the ions of the metal. This oscillatory dipole moment causes an oscillatory polarization $\mathbf{P} = P_0 \exp(i\omega t)$ where the electric permittivity of the metal is defined as [3]

$$\epsilon_m = 1 - \frac{\omega_p^2}{(\omega^2 + i\gamma_m\omega)}. \tag{1.1}$$

Parameter $\omega_p = \sqrt{(ne^2/m_e\epsilon_0)}$ is defined as the plasmon frequency. Metallic damping corresponds to γ_m while vacuum permittivity is denoted as ϵ_0 and $i = \sqrt{-1}$. A visual representation of the permittivity is seen in Figure 1.1. Electric permittivity is zero when frequency is equal to metal's plasmon frequency. Note how the electric permittivity becomes negative when the frequency is less than the metal's plasmon frequency. This will become important in the following section.

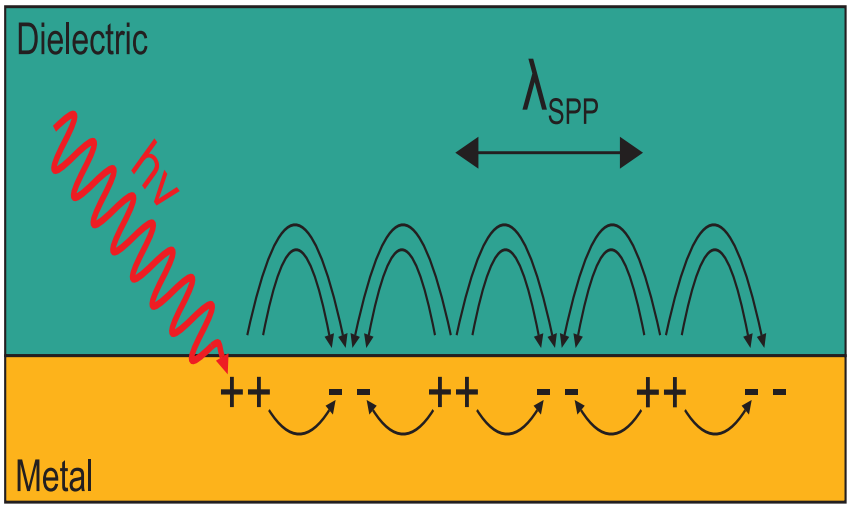

Figure 1.2: Schematic illustration of an surface plasmon polariton propagating along a metal-dielectric interface. These waves can be excited by an electromagnetic light with E=hv.

1.2 Surface Plasmon Polaritons

Polaritons are bosonic particles which arise from a strong coupling between electromagnetic fields with an electric or magnetic dipole excitation. Coupling occurs when the two dispersion relationships of light and the excitation are in the same path of each other and have the same energy [4]. Surface plasmon polaritons are evanescently confined electromagnetic oscillation in the perpendicular direction and propagating along an interface between a dielectric and a conductor. Surface plasmon polaritons form due to the coupling between a conductor's surface plasmon with an applied electromagnetic field. Figure 1.2 give a visual illustration of surface plasmon polaritons.

Consider a simple flat single interface between a dielectric and a conductor with electric permittivities ϵ_d and ϵ_m respectively. Solving boundary conditions for the propagating transverse magnetic solutions at the interface with the components of the wave vector perpendicular to the interface of the dielectric and the metal k_d and k_m, respectively, yields [3]

$$\frac{k_m}{k_d} = -\frac{\epsilon_m}{\epsilon_d}. \tag{1.2}$$

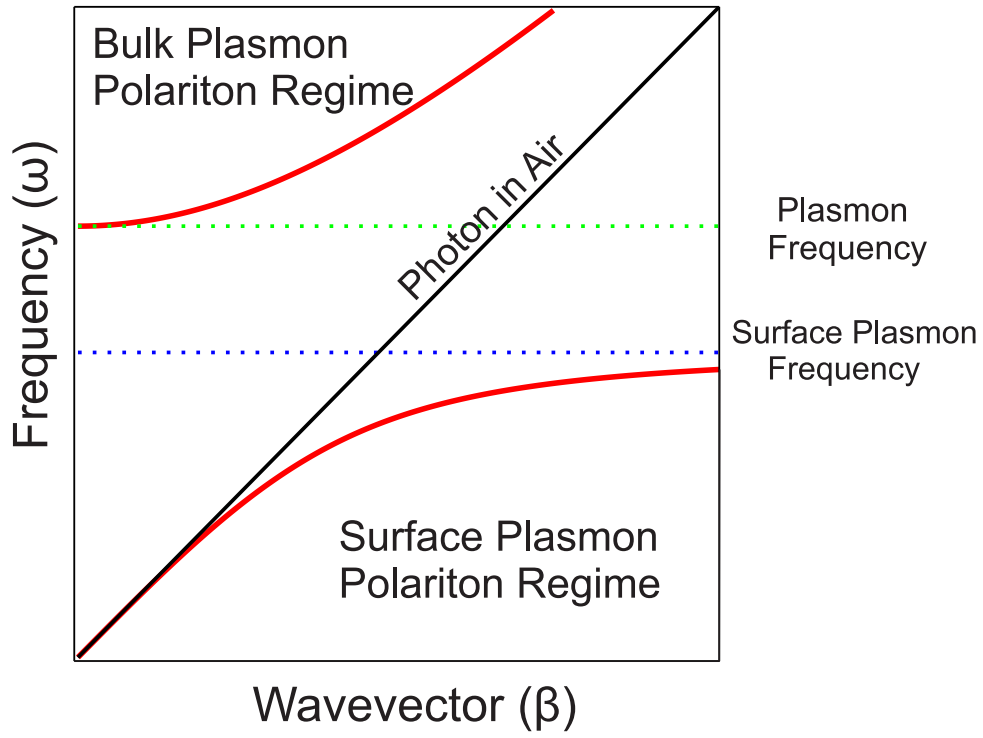

Figure 1.3: Dispersion relation of plasmon polaritons within a metal-dielectric system. The lower curve corresponds to the surface plasmon polaritons where the limit corresponds to the surface plasmon polariton frequency. The higher curve indicates the plasmon polaritons found in the bulk metal, and the lower limit of this curve indicates plasmon frequency of the metal.

Notice the negative sign in the expression above. This negative quantity arises because of the negatives found in the exponents when solving the boundary conditions (x=0). Thus for surface plasmon polaritons to exist the real part of electric permittivities must be opposite signs between materials at the interface. For this reason surface plasmon polaritons only exist between conductors/metals and dielectric materials. Further solving the wave equations gives

$$k_d^2 = \beta^2 - \left(\frac{\omega}{c}\right)^2 \epsilon_d \tag{1.3}$$

$$k_m^2 = \beta^2 - \left(\frac{\omega}{c}\right)^2 \epsilon_m. \tag{1.4}$$

The dispersion relation of the surface plasmon polariton propagating at the interface, β, is

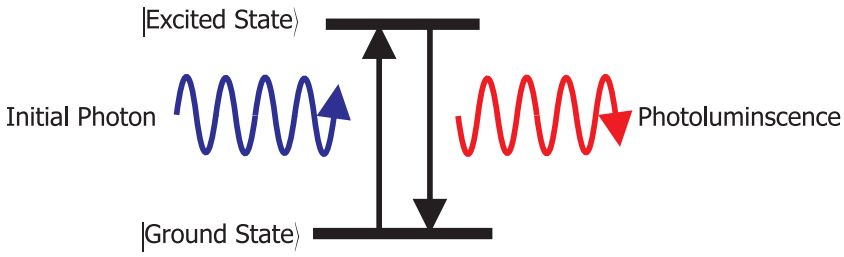

Figure 1.4: Illustration of the photoluminescence process. An initial photon causes an excitation, after some time a photon is released due a decay from the excited state to the ground.

determined by combining equations (1.2-1.4) resulting [3]

$$\beta = \left(\frac{\omega}{c}\right)\sqrt{\frac{\epsilon_d \epsilon_m}{\epsilon_d + \epsilon_m}} \tag{1.5}$$

Solving the transverse electric solutions will show that no surface plasmon modes exist. Therefore, surface plasmon polaritons only occur with transverse magnetic waves. Figure 1.3 is a graphical representation of the dispersion relation of surface plasmon polariton. In this figure consider a conductor with negligible metallic damping γ_m. Notice the two curves, the first correspond to the surface plasmon polariton while the higher frequency second curve corresponds to the bulk plasmon polariton. The lower curve goes to a horizontal limit which is characterized as the surface plasmon frequency. Most research occurs in near this frequency. Surface plasmon polaritons can exist in any dielectric-metallic like structure. Examples of metallic like structures are metallic nanoparticle, metamaterial made with metals, and metallic graphene.

1.3 Photoluminescence

When working with electromagnetic waves precise measuring is required. One method highly used in research is evaluating the photoluminescence of the system. Photoluminescence is light emission from any matter after an initial photon was absorbed to excite the state. It is one form of luminescence. Initially a photon is absorbed which causes an energy transition between a ground state to an excited state. In quantum mechanics the absorbed photon must have energy

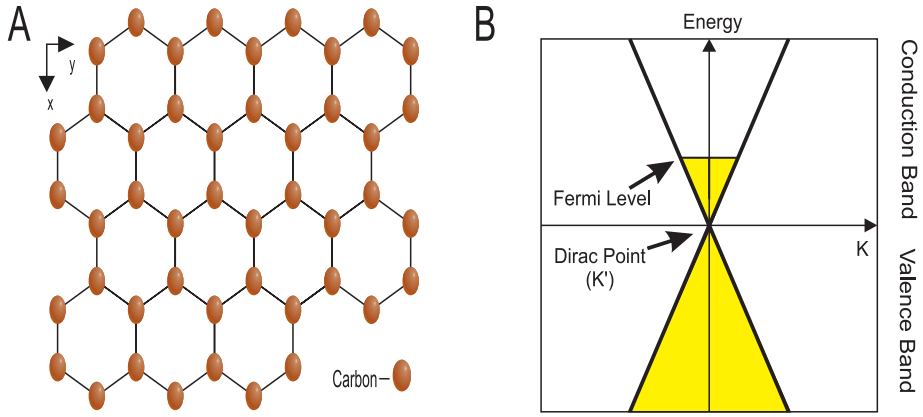

Figure 1.5: A.)Schematic representation of a 2D graphene lattice. Vertices correspond to individual carbon atom. b.) Dispersion relation of a 2d graphene lattice. The Dirac point is the overlapping point between graphene's conductions and valence band. The fermi level is above the Dirac point thus the carriers are electronic like [3].

equal to that of the transition energy. After the excitation process occurs the system goes into a relaxation phase where other photons are typically radiated out. The emitted energy is not necessarily equal to the original absorbed photon. The time period between full excitation to complete relaxation depends on the decay rate which is governed by Fermi's golden rule [5].

1.4 Graphene

The exploitation of existing material in efforts to develop optoelectronic devices has seen some large interest due to the numerous potential possibilities. Graphene, an allotrope of carbon, is considered to be one of the larger researched areas in condensed matter for its exotic properties. Graphene is a two-dimensional carbon structure composed of a hexagonal lattice where each vertex is a carbon atom. A diagram of this hexagonal lattice is shown in Figure 1.5A.

Graphene has numerous exotic properties. It has been claimed as being one of the strongest materials in the world [6]. Other physical properties of graphene are: transparency, light weight, bendability and being harder than diamond, which is another allotrope of carbon. Graphene has shown to have fascinating electric, magnetic, and heat properties. It is an excellent conductor, much better than copper, and graphene can also be a great semiconductor

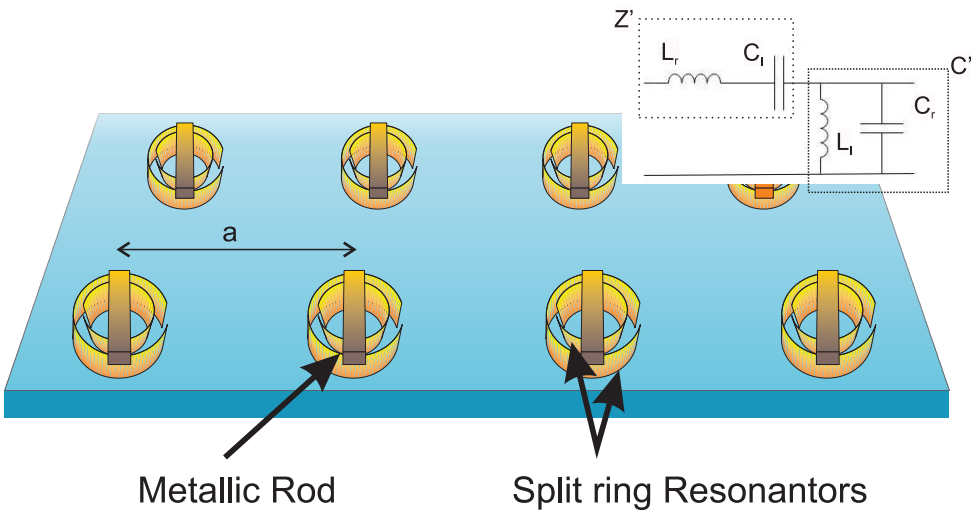

Figure 1.6: A metamaterial structure consisting of an array of metallic split ring resonators and metallic rod. Inset: An equivalent L-C electric circuit schematic of the unit cell.

[7]. Metallic graphene is represented in Figure 1.5B. When the fermi level is above the Dirac point graphene resembles metallic properties, with electron like carriers. With such properties graphene has been implemented in a variety of research areas spanning from aerospace, automotive, electronics, sensors, solar, power storage.

1.5 Metamaterials

Striving to develop better optoelectronic devices, and having exhausted possible uses of natural materials, researchers have come to devise artificial materials for the properties they need. One type of artificial material researchers use are metamaterials. Metamaterials stem from the Greek word meta which means 'beyond'. These materials are developed to find properties that are not found or are beyond nature. These structure are composed of repeating unit cells, and compared to the wavelength of the applied wave are much smaller. Thus the applied wave only interacts with a new homogeneous material that has tunable properties based on both the composition of the material and of the entirely new structure.

Metamaterials have some of the most unique abilities seen in science. They possess the

ability to have both negative permeability and permittivity simultaneously. This trait has led to the concept of developing physical cloaking devices seen in fiction, and desired by all militaries throughout history. Metamaterials have been studied since the late 1960s where a Russian physicist developed theoretical work on both negative permeability and permittivity substances [8]. However, it was not until recent years groups actually develop these first types of structures.

The unit cells of metamaterials can be composed with a variety of structure and used for different application such as electromagnetism, acoustics, and mechanics motion. In electromagnetism, there are three popular metamaterial structures. The first structure is composed of split ring resonators and metallic rods (seen in Figure 1.6), the second is composite right handed and left handed metamaterials, while the third method is a metallic nano-hole array structure. Methods consist of interdigital capacitors and shunt stub inductors. In the inset of Figure 1. 6 consists of an inductance per length Z' and a capacitance per length C'. Inductance per length can be represented as an shunt inductance per unit length L_r in series with a capacitance time unit length C_l, while C' is represented as an inductance time unit length L_l in parallel with a shunt capacitance per unit length C_r [9]. This is called the transmission line method used by engineers. Using this method allows researchers to evaluate the dispersion relation of the metamaterial.

1.6 Quantum Emitters

With our urge to develop small devices, smaller building components must be engineered. Quantum emitters have been used for the development of new light sources in many fields such as, optoelectronic devices, LEDs, chemical and biological probes and labels. Quantum emitters can be single molecules, quantum dots, biological and chemical dyes. Quantum dots will be prevalently used in this thesis.

Quantum dots are nanostructures that were developed in the 1980s and are now present in

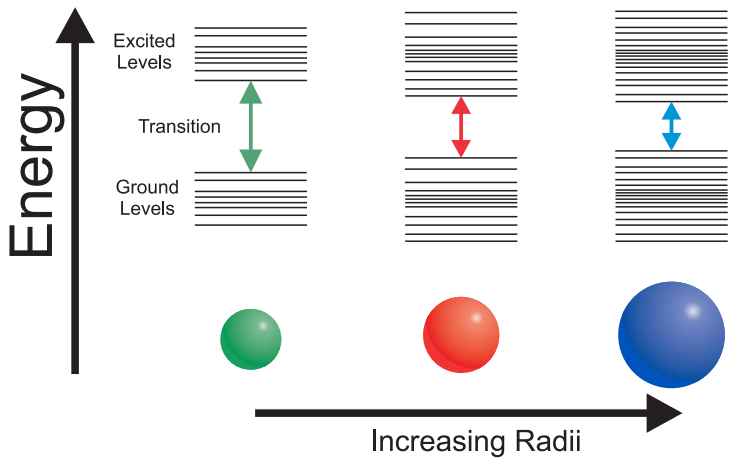

Figure 1.7: Splitting energy levels in semiconductor quantum dots due to quantum energy levels. Band gaps decrease as quantum dots increase in size.

our hi-tech LED televisions. Quantum dots are semiconductor nanostructures where excitons are confined in all three spatial directions. Typical diameters of quantum dots lie between 10 to 50nm in size, corresponding to 10 to 50 atoms in diameter and a total of 100 to 100,000 atoms within the volume of the structure [10]. Quantum dots have electronic characteristics, such as discrete energy states and electronic band gaps. These characteristics are highly tunable due to the fact that they are closely linked with the size and the shape of the structure. Figure 1.5 illustrates the tunability of these semiconductors.

1.7 Density Matrix Method

In quantum mechanics, experimental physics parameters are calculated by taking the average of an operator. The density matrix method is used to evaluate the average of an operator. The density matrix is a matrix that describes a quantum system in a mixed state of a statistical ensemble of several quantum states [11].

$$\langle O \rangle = Tr(O\rho) \tag{1.6}$$

$$\langle O \rangle = \sum_{n=1}^{\infty} \langle \Phi_n | O\rho | \Phi_n \rangle \tag{1.7}$$

Here the average of an operator O is taken over density matrix operator ρ, with Φ_n as an orthonormal set. The density matrix operator corresponds to

$$\rho = |\Psi_n\rangle\langle\Psi_n| \tag{1.8}$$

Solving the equation of motion for the density matrix, by using the time dependent Schrodinger equation and its Hermitian conjugate results in the von Neumann Equation [11]

$$-i\hbar \frac{\partial \rho}{\partial t} = [H, \rho] \tag{1.9}$$

This equation will be solve in each chapter.

In this thesis we consider hybrid systems which are made of two or more nanocomposites. These hybrid system interact with external light and other components of the system. Hence the Hamiltonian of these hybrids will be presented in their subsequent chapters.

Bibliography

[1] S.A. Maier, Plasmonics: Fundamentals and Applications (2007).

[2] D.R. Mason, S.G. Menabde, S. Yu, and N. Park, Sci. Rep. 4, 4536 (2014).

[3] M.R. Singh, Electronic, Photonic, Polaritonic, and Plasmonic Materials (Wiley Customs, Toronto, 2014).

[4] A. V. Zayats and I.I. Smolyaninov, J. Opt. A Pure Appl. Opt. 5, S16 (2003).

[5] L. Schiff, Quantum Mechanics (Pure & Applied Physics) (McGraw-Hill, New York, 1968).

[6] C. Lee, X. Wei, J.W. Kysar, J. Hone, and =, Science (80-.). 321, 385 (2008).

[7] A.H.. Castro Neto, N.M.R.. Peres, K.S.. Novoselov, A.K.. Geim, and F. Guinea, Rev. Mod. Phys. 81, 109 (2009).

[8] V.G. Veselago, Sov. Phys. Uspekhi 509, 509 (1968).

[9] C. Caloz and T. Itoh, Electromagnetic Metamaterials: Transmission Line Theory and Microwave Applications: The Engineering Approach (2005).

[10] T. Masumoto, Yasuaki Takagahara, Semiconductor Quantum Dots (Springer Berlin Heidelberg, Berlin, Heidelberg, 2002).

[11] M.R. Singh, Advance Quantum Physics (Wiley Customs, Toronto, 2014).

Chapter 2

Introduction

In the previous section we discussed some fundamental information which will be beneficial to the reader in order to understand this thesis. Specifically, quantum dots, metamaterials and the density matrix were addressed in the previous chapter. The objective of this chapter is to present an overview of the literature works covering concepts discussed in the thesis.

2.1 Photoluminescence Quenching in Graphene Hybrid Nanosystems

There is an appreciable interest in the study of the optical properties of nanoscale hybrid systems made from nanosystems such as quantum emitter, metallic nanoparticles and graphene [1-12]. Quantum emitters can be a semiconductor quantum dot, chemical dye, graphene quantum dot and a biological/chemical molecule. Research in optical properties, such as photoluminescence, in these systems has shown great importance due to its applications in optical switching, biomolecular sensing and imaging [1, 2]. Many groups have studied the photoluminescence in quantum dot and metallic nanoparticle hybrids [3-9]. For instance, photoluminescence has been measured in CdTe quantum dots and copper metallic nanoparticle hybrids by Chan et al. [5]. They found that the intensity of the photoluminescence in the quantum dot has been

quenched due to the presence of the copper nanoparticles. Their results suggested that these quantum dots can be used as probes for ultrasensitive copper nanoparticle detection. Similarly, photoluminescence quenching has also been seen in quantum dot gold and metallic nanoparticle hybrids by Oh et al. [6]. Here, they imply that the system can be used for gold detection in biomolecules. It is known that lead is a hazardous heavy metal and that is also very toxic. Wu et al. [7] suggested that the photoluminescence quenching mechanism in the quantum dots can be used to detect hazardous heavy metals, such as lead.

Some effort has been devoted to study the photoluminescence in graphene hybrid systems [10-12]. For example, Kasry et al. [10] have studied the quenching on CY5 dye and graphene. Their results indicate this effect was one order of magnitude higher than that of gold. Here the CY5 dye acts as a quantum emitter. Photoluminescence quenching has also been observed in hybrid systems made from graphene and metallic nanoparticles. Nanoprobes for silver metallic nanoparticles have been constructed using photoluminescence quenching techniques in graphene [11]. Photoluminescence quenching has been seen in quantum dot and graphene hybrids [12].

Photoluminescence quenching has been observed in other systems [13-22]. Lui et al. [13] has studied the photoluminescence quenching between unbounded gold metallic nanoparticles and graphene quantum dots. Their results show florescence gradually decrease with the increase of gold metallic nanoparticle concentration. Quantum dot and DNA hybrid systems are used to detect different based DNA [15]. Jung et al. [16] observed that when immobilized antibodies on graphene oxide captured a virus cell (target) photoluminescence quenching was detected, which illustrates the use for detection of viruses. Fan et al. [17] prepared graphene quantum dot-TNT hybrid system, and found photoluminescence quenching when the graphene quantum dots were in the vicinity of the explosive compound TNT. This system can be used for ultrasensitive detection of TNT. Composite quantum dots such as CdSe-ZnS have also seen photoluminescence quenching when in the vicinity of antibiotics [17].

2.2 Photoluminescence Quenching in Metamaterial Nanosystems

In recent years, optical studies in artificial nanoscale hybrid systems have had great interests due to the numerous optical properties these systems can hold. One type of artificial materials which has compelling possibilities are metamaterials. Metamaterials are artificially engineered structures for which the properties of these materials are partly based upon the original compositions and of the newly designed structures. Research in metamaterials has shown great importance due to its applications in superlenses, medical sensing, and telecommunication [23-29]. Large areas of metamaterial research involve exploiting the zero and negative index of refraction feasibility. Recently, Yang et al. has fabricated an on-chip integrated metamaterial with a refractive index of zero in the optical regime, which is applicable in integrated optics [23]. The team used a low-aspect-ratio silicon pillar arrays embedded in a polymer matrix and cladded by gold films. Negative index metamaterials have shown interesting results in deflecting electromagnetic waves, and researchers have developed many methods forming these materials. Chanda et al. formed a negative index metamaterial by nanotransfer printing which has shown strong negative index of refraction in near-infrared spectral range [24]. For negative index materials to exist, the material must possess the ability to have both negative permittivity and permeability. In noble metals, negative permittivity allows for the existence of surface plasmon polaritons which play a crucial role in energy transfer, photoluminescence quenching and other optoelectronic device applications.

Photoluminescence plays an important part in nanooptics research due to the numerous applications in optoelectronic devices. Photoluminescence has been extensively studied in hybrid systems composed of quantum emitters, quantum dots and biomolecular dyes, with metallic nanoparticles and/or graphene [30-34] as seen in the previous section. Matsumoto and group observed photoluminescence quenching in a system with CdSe-ZnS quantum dots in the presence of a gold nanoparticle film [34]. They produced a system with a reduced blinking

and non-blinking characteristics which would prove to be valuable in bioanalytical detection. Photoluminescence has applications in detecting cancer markers [35]. Her2 and other cancerous cellular targets have been focused by photoluminescence labeling technique from Wu X et al., using semiconductor quantum dots as florescent labels for cellular imaging. Their results demonstrated that quantum dot- based probes can be effective in cellular imaging. Another large area in photoluminescence research has been in systems made with one of the largest interests in condensed matter; graphene [36]. Zeng et al. measured photoluminescence intensity in quantum dot, gold nanoparticle and graphene hybrid system, and noticed that the photoluminescence intensity of the quantum dot was quenching in the presence of gold nanoparticle and graphene. The group also studied how the addition of antigens to quantum dot binding sites decreased quenching effects due to impeding the distance between the quantum dot and the gold nanoparticle and graphene, indicating a biomolecular marker.

Metamaterials, similar to noble metals, have the ability to form SPPs, thus allowing a variety of optoelectronic properties in hybrid systems, such as photoluminescence. The work on these materials has been researched but it has not seen the same amount of research as the other materials seen above. With such a wide range of exotic properties, groups have started focusing on photoluminescence properties in metamaterial systems [37-38]. Metamaterials alone possess the possibility for photoluminescence research. Skreekanth et al. developed an indefinite metamaterial based on Au/Al203 multilayer structure, for which they found the increase of Au/Al2O3 layers quenched the photoluminescence [37]. For a more tunable system, hybrid systems with a metamaterial have also been researched. Krishnamoorthy et al. reported an enhancement in spontaneous emission from CdSe/ZnS core-shell quantum dot by exploiting nonmagnetic metamaterial structure [38]. Photoluminescence in metamaterial hybrid systems have also seen enhancement. Tanaka et al, worked with a gold film metamaterial and noticed that a multifold intensity increase and narrowing of their photoluminescence [39]. However, even though there are experiments with these systems, theoretical work is much fewer.

2.3 Plasmonics in Metamaterial Nanosystems

There is considerable interest in developing nanoscale plasmonic devices, used for sensing, by combining metamaterials with quantum dots into hybrid nanostructures [40-48]. Metamaterials come in a variety of shapes and structures. For hybrid system structures to be classified as a metamaterial, the wavelength applied onto the system is much larger than the unit cell of the structure. Here, we consider a metamaterial made out of gold comprised of an array of nanoholes. To study the light-matter interaction in quantum dots and metamaterials the hybrid systems are deposited on a dielectric crystal as a substrate. Examples of dielectric materials are Pyrex, RT Duroid and PMMA. Without the dielectric substrate, surface plasmon polaritons would not exist. Surface plasmon polaritons are needed to study light-matter interactions. The properties of the surface plasmon polaritons depend on the dielectric constant between the NAS and the surrounding dielectric medium.

Most research on plasmonics has focused mainly on noble metals [49-53]. Research in noble metal hybrids is concentrated in nanophotonic applications such as integrated photonic systems [54-57], biosensing [58, 59] photovoltaic devices [60,61] and single photon transistors for quantum computing [62]. Many applications of noble metal plasmonics are realized in the visible to near-infrared frequencies.

The problem with the noble metals is that they are hardly tunable and exhibit large Ohmic losses, which limit their applicability to plasmonic and optoelectronic devices. On the other hand, metamaterials provide an attractive alternative to noble metal plasmons. Metamaterials provide the capability to exhibit properties not seen in nature. Optical properties of metamaterials depend on the properties and of nanoscale organization of the atomic composites. This allows for a much tighter confinement, small Ohmic losses and relatively long propagation distances compared to noble metals. The surface plasmon polaritons in metamaterials can also be tuned due to the flexibility of metamaterials.

Plasmonic properties of metamaterial systems have been studied experimentally [40-43]. For example, cut-out structures in a thin gold film have been synthesized to study electro-

magnetically induced transparency for localized surface plasmon resonance plasmonic sensing [40]. Metamaterials consisted of an ultra thin semiconducting layer topped a with solid nanoscopically perforated metallic film, and a dielectric interference film was fabricated to absorb electromagnetic radiation in the visible range, for a high-efficient solar cell [41]. Similarly, it is shown that using DNA to design plasmonic metamaterials with tunable optical properties allows for the potential development of optical circuitry, optical cloaking and data exchange [42]. Cadmium selenide quantum dots and silver nanogap metamaterials were fabricated to study the photoluminescence [43]. Finally, metamaterial systems have also been fabricated by several groups [45-48] to study other sensing possibilities of these hybrid systems. Research on metamaterial hybrid nanostructures could also lead to applications in quantum computing and communication as well as numerous applications in biophotonics and sensing.

2.4 Objective and Outline of the Thesis

The objective of this thesis is to study the quantum optics of plasmonic nanosystems, which could lead to the development of new optoelectronic devices. These nanosystems are developed by combining two or more nanocomponents into one cohesive system. Each nanocomponent contains particular optical and electrical properties. These new cohesive nanosystems result in unique optical and electrical properties that surpass the capabilities of its individual nanocomponents. Medical advances have seen great improvements in recent history; however further advancements have hit an obstacle when developing devices for the nanoscale. The problem with electronic devices is that they are reaching their efficiency and speed thresholds. The ambition of this thesis is to study switching mechanisms, similar to those found in the thesis. These switching mechanisms can be applied to making new optoelectronic devices, for nanosensing, that can operate at better efficiencies and speed for nanoscale. From our models, changes in optical responses can be used to detect desired substances or determine optical or electronic properties. In this thesis, optical properties are theoretically investigated for several

types of plasmonic nanosystems.

The thesis is organized as follows: In Chapter 3, we developed a theory for energy transfer and study plasmonic properties in hybrid nanosystems made from two and three nanocomposites. We consider that our nanosystems are comprises of quantum emitters, metallic nanoparticles and graphene. The metallic nanoparticles and graphene have surface plasmons which couple with probe photons to create surface plasmon polaritons. Therefore, the excitons in the quantum emitters interact with surface plasmon polaritons via the exciton-SPPs interaction. Due to this interaction, energy is exchanged between the nanosystems. The second quantized formulation and the quantum density matrix method have been used to calculate the expression of photoluminescence and the radiative and nonradiative decay processes in the presence of exciton-SPPs interaction. We have compared our theory with experiments of two and three nanosystems, and a good agreement between theory and experiments is achieved. It is found that the photoluminescence quenching in hybrid systems made from quantum emitter, metallic nanoparticles and graphene not only occurs through the direct nonradiative energy transfer from the quantum emitter to the metal nanoparticle and to graphene, but also occurs through the indirect nonradiative energy transfer from quantum emitter to the metal nanoparticle via graphene and from the quantum emitter to graphene via metal nanoparticle. These are interesting findings and they can be used to fabricate nanoswitches and nanosensors for medical applications.

In Chapter 4, we developed a theory for photoluminescence quenching of semiconductor quantum dot doped in metallic nanoparticle and split-ring metamaterial hybrid system, including local fields. The split-ring metamaterial lies on top of a dielectric substrate where within the dielectric substrate is doped with quantum dots and metallic nanoparticle near the interface. Results show that photoluminescence quenching decreases as distance between segments becomes further apart, when the excitons of the quantum dot resonant with surface plasmon polaritons of split-ring metamaterial and metallic nanoparticle. Our results also show that an increase in direct field distance has a drastic effect on photoluminescence quenching compared

to an increase indirect field distances. Consistencies are found between similar experimental studies and our results. Based on this study, new types of optoelectronic devices for imagining, sensing, and switching for the nanoscale can be developed.

In Chapter 5, we investigate the light-matter interaction in quantum dots and a metamaterial, composed of a nanohole array structure, deposited on a dielectric substrate Pyrex. A probe laser field is applied to measure the absorption coefficient in the quantum dot. The probe laser induces surface plasmons and couples with these plasmon to produce surface plasmon polaritons. Using the density matrix method, we have calculated the absorption coefficient of the quantum dot in the presence of exciton-SPPs couplings. When the exciton energy of the quantum dot is resonant with the surface plasmon polariton energies, the absorption in the quantum dot is enhanced in the visible range. The enhancement is due to the transfer of surface plasmon polariton energies from the metamaterial to the quantum dot. Furthermore, when the exciton energy is non-resonant with the surface plasmon polariton energies, the enhancement of the absorption disappears. In other words, the energy transfer from the metamaterial to the quantum dot can be switched ON and OFF by mismatching the resonant energies of excitons and polaritons. The mismatching of energies can be achieved by applying external pump lasers or stress and strain fields. These are interesting findings, and they can be used to fabricate switches and sensors in the visible energy range.

Finally, in the last chapter, we have our concluding remarks summarizing the thesis and discussing potential future research.

Bibliography

[1] N. Varghese, U. Mogera, A. Govindaraj, A. Das, P.K. Maiti, A.K. Sood, and C.N.R. Rao, ChemPhysChem 10, 206 (2009)

[2] C.H. Lu, H.H. Yang, C.L. Zhu, X. Chen, and G.N. Chen, Angew. Chemie - Int. Ed. 48, 4785 (2009).

[3] J.D. Cox, M.R. Singh, G. Gumbs, M.A. Anton, and F. Carreno, Phys. Rev. B - Condens. Matter Mater. Phys. 86, (2012).

[4] S.G. Kosionis, A.F. Terzis, V. Yannopapas, and E. Paspalakis, J. Phys. Chem. C 116, 23663 (2012).

[5] Y.H. Chan, J. Chen, Q. Liu, S.E. Wark, D.H. Son, and J.D. Batteas, Anal. Chem. 82, 3671 (2010).

[6] E. Oh, M.-Y. Hong, D. Lee, S.-H. Nam, H.C. Yoon, and H.-S. Kim, J. Am. Chem. Soc. 127, 3270 (2005).

[7] H. Wu, J. Liang, and H. Han, Microchim. Acta 161, 81 (2008).

[8] M. Li, X. Zhou, S. Guo, and N. Wu, Biosens. Bioelectron. 43, 69 (2013).

[9] T. Pons, I.L. Medintz, K.E. Sapsford, S. Higashiya, A.F. Grimes, D.S. English, and H. Mattoussi, Nano Lett. 7, 3157 (2007).

[10] A. Kasry, A.A. Ardakani, G.S. Tulevski, B. Menges, M. Copel, and L. Vyklicky, J. Phys. Chem. C 116, 2858 (2012).

[11] Y. Wen, F. Xing, S. He, S. Song, L. Wang, Y. Long, D. Li, and C. Fan, Chem. Commun. (Camb). 46, 2596 (2010).

[12] H. Dong, W. Gao, F. Yan, H. Ji, and H. Ju, Anal. Chem. 82, 5511 (2010).

[13] Y. Liu, W.Q. Loh, A. Ananthanarayanan, C. Yang, P. Chen, and C. Xu, RSC Adv. 4, 35673 (2014).

[14] C.H. Lui, K.F. Mak, J. Shan, and T.F. Heinz, Phys. Rev. Lett. 105 (2010).

[15] R. Freeman, X. Liu, and I. Willner, J. Am. Chem. Soc. 133, 11597 (2011).

[16] J.H. Jung, D.S. Cheon, F. Liu, K.B. Lee, and T.S. Seo, Angew. Chemie - Int. Ed. 49, 5708 (2010).

[17] L. Fan, Y. Hu, X. Wang, L. Zhang, F. Li, D. Han, Z. Li, Q. Zhang, Z. Wang, and L. Niu, Talanta 101, 192 (2012).

[18] Z. Liu, P. Yin, H. Gong, P. Li, X. Wang, and Y. He, J. Lumin. 132, 2484 (2012).

[19] M. Noh, T. Kim, H. Lee, C.K. Kim, S.W. Joo, and K. Lee, Colloids Surfaces A Physicochem. Eng. Asp. 359, 39 (2010).

[20] D. Pan, J. Zhang, Z. Li, and M. Wu, Adv. Mater. 22, 734 (2010).

[21] G. Eda, Y.Y. Lin, C. Mattevi, H. Yamaguchi, H.A. Chen, I.S. Chen, C.W. Chen, and M. Chhowalla, Adv. Mater. 22, 505 (2010).

[22] F. Bonaccorso, Z. Sun, T. Hasan, and a. C. Ferrari, 4, 611 (2010).

[23] Y. Li, S. Kita, P. Muoz, O. Reshef, D.I. Vulis, M. Yin, M. Lonar, and E. Mazur, Nat. Photonics 9, 738 (2015).

[24] D. Chanda, K. Shigeta, S. Gupta, T. Cain, A. Carlson, A. Mihi, A.J. Baca, G.R. Bogart, P. Braun, and J.A. Rogers, Nat. Nanotechnol. 6, 402 (2011).

[25] C.L. Cortes, W. Newman, S. Molesky, and Z. Jacob, J. Opt. 14, 063001 (2012).

[26] A. Poddubny, I. Iorsh, P. Belov, and Y. Kivshar, Nat. Photonics 7, 948 (2013).

[27] S. V Zhukovsky, T. Ozel, E. Mutlugun, N. Gaponik, A. Eychmuller, A. V Lavrinenko, H. V Demir, and S. V Gaponenko, Opt. Express 22, 18290 (2014).

[28] S.P. Rodrigues, Y. Cui, S. Lan, L. Kang, and W. Cai, Adv. Mater. 1124 (2014).

[29] W.D. Newman, C.L. Cortes, and Z. Jacob, J. Opt. Soc. Am. B-Optical Phys. 30, 766 (2013).

[30] A. Samanta, Y. Zhou, S. Zou, H. Yan, Y. Liu, P. Long, and R. Spectroscopic, Nano Lett. (2014).

[31] I.-S. Liu, H.-H. Lo, C.-T. Chien, Y.-Y. Lin, C.-W. Chen, Y.-F. Chen, W.-F. Su, and S.-C. Liou, J. Mater. Chem. 18, 675 (2008).

[32] L. Li, G. Wu, T. Hong, Z. Yin, D. Sun, E.S. Abdel-Halim, and J.J. Zhu, ACS Appl. Mater. Interfaces 6, 2858 (2014).

[33] Y. Li, Y. Hu, Y. Zhao, G. Shi, L. Deng, Y. Hou, and L. Qu, Adv. Mater. 23, 776 (2011).

[34] Y. Matsumoto, R. Kanemoto, T. Itoh, S. Nakanishi, M. Ishikawa, and V. Biju, J. Phys. Chem. C 112, 1345 (2008).

[35] X. Wu, H. Liu, J. Liu, K.N. Haley, J.A. Treadway, J.P. Larson, N. Ge, F. Peale, and M.P. Bruchez, Nat. Biotechnol. 21, 41 (2003).

[36] X. Zeng, S. Ma, J. Bao, W. Tu, and Z. Dai, Anal. Chem. 85, 11720 (2013).

[37] K.V. Sreekanth, A. De Luca, and G. Strangi, Sci. Rep. 3, 3291 (2013).

[38] H.N. Krishnamoorthy, Z. Jacob, E. Narimanov, I. Kretzschmar, and V.M. Menon, in OSA/CLEO/QELS 2010 (2010), p. JWA23.

[39] K. Tanaka, E. Plum, J.Y. Ou, T. Uchino, and N.I. Zheludev, Phys. Rev. Lett. 105, 351 (2010).

[40] N. Liu, T. Weiss, M. Mesch, L. Langguth, U. Eigenthaler, M. Hirscher, C. S??nnichsen, and H. Giessen, Nano Lett. 10, 1103 (2010).

[41] Y. Wang, T. Sun, T. Paudel, Y. Zhang, Z. Ren, and K. Kempa, Nano Lett. 12, 440 (2012).

[42] K.L. Young, M.B. Ross, M.G. Blaber, M. Rycenga, M.R. Jones, C. Zhang, A.J. Senesi, B. Lee, G.C. Schatz, and C.A. Mirkin, Adv. Mater. 26, 653 (2014).

[43] L.N. Tripathi, T. Kang, Y.-M. Bahk, S. Han, G. Choi, J. Rhie, J. Jeong, and D.-S. Kim, Opt. Express 23, 14937 (2015).

[44] Z. Fei, G.O. Andreev, W. Bao, L.M. Zhang, A. S. McLeod, C. Wang, M.K. Stewart, Z. Zhao, G. Dominguez, M. Thiemens, M.M. Fogler, M.J. Tauber, A.H. Castro-Neto, C.N. Lau, F. Keilmann, and D.N. Basov, Nano Lett. 11, 4701 (2011).

[45] T. Chen, S. Li, and H. Sun, Sensors 12, 2742 (2012).

[46] Z.G. Dong, H. Liu, J.X. Cao, T. Li, S.M. Wang, S.N. Zhu, and X. Zhang, Appl. Phys. Lett. 97, (2010).

[47] I.A.I. Al-Naib, C. Jansen, and M. Koch, Appl. Phys. Lett. 93, (2008).

[48] J.F. OHara, R. Singh, I. Brener, E. Smirnova, J. Han, A.J. Taylor, and W. Zhang, Opt. Express 16, 1786 (2008).

[49] M. Achermann, J. Phys. Chem. Lett. 1, 2837 (2010).

[50] R.D. Artuso and G.W. Bryant, Phys. Rev. B - Condens. Matter Mater. Phys. 82, (2010).

[51] S.M. Sadeghi, L. Deng, X. Li, and W.-P. Huang, Nanotechnology 20, 365401 (2009).

[52] M.-T. Cheng, S.-D. Liu, H.-J. Zhou, Z.-H. Hao, and Q.-Q. Wang, Opt. Lett. 32, 2125 (2007).

[53] M. Durach, A. Rusina, V.I. Klimov, and M.I. Stockman, New J. Phys. 10, (2008).

[54] J.M. Luther, P.K. Jain, T. Ewers, and A.P. Alivisatos, Nat. Mater. 10, 361 (2011).

[55] D.K. Gramotnev and S.I. Bozhevolnyi, Nat. Photonics 4, 83 (2010).

[56] L. Novotny and N. van Hulst, Nat. Photonics 5, 83 (2011).

[57] J.A. Schuller, E.S. Barnard, W. Cai, Y.C. Jun, J.S. White, and M.L. Brongersma, Nat. Mater. 9, 193 (2010).

[58] a V Kabashin, P. Evans, S. Pastkovsky, W. Hendren, G. a Wurtz, R. Atkinson, R. Pollard, V. a Podolskiy, and a V Zayats, Nat. Mater. 8, 867 (2009).

[59] H.X. Xu, E.J. Bjerneld, M. Kll, and L. Brjesson, Phys. Rev. Lett. 83, 4357 (1999).

[60] H.A. Atwater and A. Polman, Nat. Mater. 9, 205 (2010).

[61] D.E. Chang, A.S. Srensen, E.A. Demler, and M.D. Lukin, Nat. Phys. 3, 807 (2007).

[62] A. Gonzalez-Tudela, D. Martin-Cano, E. Moreno, L. Martin-Moreno, C. Tejedor, and F.J. Garcia-Vidal, Phys. Rev. Lett. 106, (2011).

Chapter 3

Photoluminescence quenching, metallic nanoparticle and graphene hybrid nanomaterials

In the previous chapter, a literature review pertaining to the topics and systems studied in this thesis was covered. In this chapter we study optical properties of quantum dots in a system with graphene and metallic nanoparticles. Photoluminescence quenching of quantum dots will be investigated when they are in the vicinity of graphene and gold metallic nanoparticles.

3.1 Introduction

The interest in the study of the optical properties of nanoscale hybrid systems made from nanosystems has seen large growth for the number of possibilities they can possess. Optical properties, such as photoluminescence (PL), in these systems has shown great importance due to its application in optical switching, biomolecular sensing and imaging [1, 2]. Recently, researchers have studied the PL in quantum emitters (QE), quantum dot (QD) and metallic nanoparticle (MNP) hybrids [6-31]. As an example, the PL has been measured in a CdTe

QD- copper MNP hybrid [7]. Here it was found that the intensity of the PL in the QD has been quenched due to the presence of the copper nanoparticles, which suggests that these QDs can be used as probes for ultrasensitive copper nanoparticle detection [7]. Optical properties of graphene (GR) nanosystem have been studied [15-18]. PL quenching has been observed in other systems [18-31]. In one systems QDs and DNA was used to detect different based DNA [20]. Researchers observed that when immobilized antibody on graphene oxide captured a virus cell (target) PL quenching was detected, which illustrates its use in the detection of viruses [22]. Composite QD such as CdSe-ZnS have also seen PL quenching when in the vicinity of antibiotics [24].

In this chapter we develop a novel theory for energy transfer and the study of plasmonics properties in a three-nanoparticle hybrid system, made from a quantum emitter (QE), MNP and GR nanosystems, using a many body quantum theory called the density matrix method. We compare our theory with experiments of the QE-MNP-GR hybrid system. In this theory the coupling of resonance energy of surface plasmon polaritons (SPPs) in MNP and GR with exciton energies in the QE play a very important role. The exciton in the QE interacts with the SPPs via the exciton-SPPs interaction which has been evaluated in the rotating wave approximation. We used the second quantized formulation and the quantum density matrix method to calculate the expression of PL and the radiative and nonradiative decay processes in the presence of exciton-SPPs interaction. Maxwell's equations in quasi-static approximation [32] have been used to calculate the polarizability of SPPs in the GR and MNP. Therefore, due to this interaction, part of the exciton energy is transferred from QE to the GR and MNP through the nonradiative process. This theory can be reduced to hybrids made from two nanosystems such as QE-MNP, QE-GR, MNP-GR. We compared our theory with PL experiments of QD-GR hybrid [17] and QD-MNP-GR hybrid [18]. A good agreement between theory and experiments is achieved. It is found that the PL quenching in QD-MNP-GR hybrid occurs through the direct nonradiative energy transfer from the QD to the MNP and GR. We have also found that PL quenching occurs through the *indirect nonradiative energy transfer* from QD to the MNP

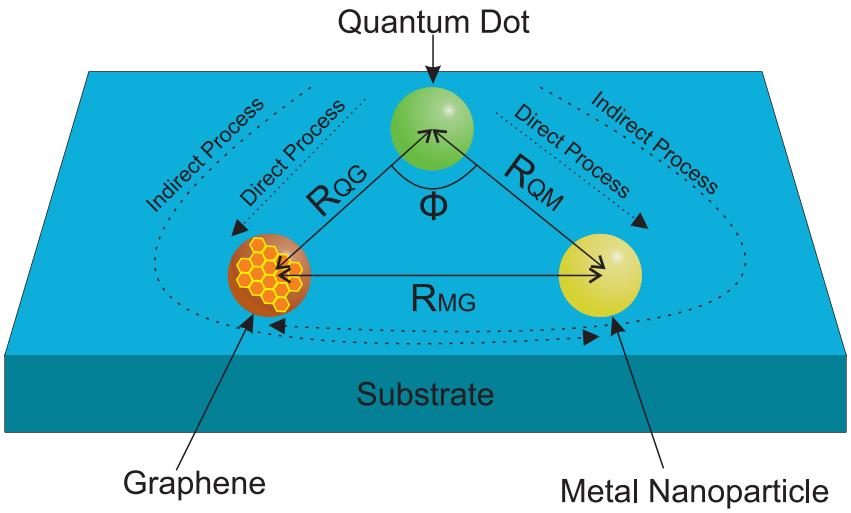

Figure 3.1: A schematic diagram of QD-MNP-GR hybrid system deposited on a liquid or solid material.

via GR and from QD to GR via MNP. These are interesting findings and they can be used to fabricate nanoswitches and nanosensors for medical applications.

3.2 Theoretical Formalism

3.2.1 Photoluminescence

The goal of this section is to develop a theory of energy transfer and the study the plasmonic effects in QE-MNP-GR hybrids. The energy exchange between nanosystems can be measured through PL experiments and an expression of the PL in the QE will be derived in the presence of coupling between excitons in the QE and SPPs in GR and MNP. A schematic diagram for the system is plotted in Figure 3-1. We consider that the hybrid system is deposited on a liquid or solid substrate. The PL process by the QE in vacuum is caused by the energy exchange from QE to the vacuum via the radiative decay of the exciton energy from the excited state of the QE to the ground state due to spontaneous emission. However, in the PL process of the QE-MNP-GR hybrid system, part of the exciton energy is transferred from the QE to the spontaneous radiative decay process and the rest of the exciton energy is transferred to the MNP and GR via

the exciton-SPPs coupling.

We applied a probe laser field in the hybrid system to monitor the PL spectrum. Due to this external field an induced exciton is created in the QE. Similarly, from this external field, induced SPPs are also created in the MNP and GR, from the coupling of surface plasmons in MNP and GR with photons of the probe field. Hence, exciton in QE interacts with SPPs of the MNP and GR.

We consider that the QE has two discrete electronic levels which are denoted as $|a\rangle$ and $|b\rangle$ where $|a\rangle$ is the ground state whereas $|b\rangle$ is the excited state. The transition frequency of an exciton for transition $|a\rangle \leftrightarrow |b\rangle$ is denoted as ω_{ab}. A probe field $E_P = E_P^0 \exp(i\omega t)$ is applied between states $|a\rangle$ and $|b\rangle$. Here E_P^0 is the amplitude and ω is the frequency of the probe field. The exciton state decays to the ground state due to the spontaneous emission process and it is denoted by Γ_{QP}, also known as the radiative decay energy loss. Excitons in the QE can also decay due to the exciton-SPPs interaction and it is represented by Γ_{NR}. This is known as the nonradiative decay energy loss. The PL spectrum of the QE can be analyzed using the following expression [33]

$$P_{PL} = Q_{PL} W_{QE} \tag{3.1}$$

where Q_{PL} is called the PL quantum yield, or the quenching factor, and is defined as

$$Q_{PL} = \left(\frac{\Gamma_{QP}}{\Gamma_{QP} + \Gamma_{NR}} \right) \tag{3.2}$$

Here the W_{QE} term is the power absorbed from the probe laser field by the QE and it is calculated as [34]

$$W_{QE} = \frac{1}{2V_Q} \mathrm{Re} \left\langle \int dV \left(E_T . \frac{dP_Q}{dt} \right) \right\rangle \tag{3.3}$$

where the volume integral is over the volume V_Q of the QE and the symbol $\langle ... \rangle$ represents the time average over the period of the applied electric field. Here E_T is the electric field falling on the QE. Parameter P_Q is the induced polarization in the QE due to the transition $|a\rangle \leftrightarrow |b\rangle$ and is found as [32] $P_Q = (\mu_{ab}\rho_{ab}) + c.c.$ where μ_{ab} and ρ_{ab} are the matrix elements of the dipole

moment operator μ and density matrix operator ρ for the transition $|a\rangle \leftrightarrow |b\rangle$, respectively. Here c.c. represents the complex conjugate. This expression of P_Q can be expressed in terms of the polarizability α_Q as

$$P_Q = \alpha_Q E_p \tag{3.4}$$

$$\alpha_Q = \frac{(\mu_{ab}\rho_{ab}) + c.c.}{E_T} \tag{3.5}$$

Putting equation (3.4) into equation (3.3), the expression of the power can be obtained as

$$W_{QE} = \frac{\omega_{ab}}{2} \mathrm{Im}\left(\alpha_Q\right) |E_T|^2 , \tag{3.6}$$

The polarizability α_Q appearing in equations (4 and 5) is calculated by using the density matrix method [35] in the next section.

Let us first calculate the electric field E_T falling on the QE. In the presence of the probe field polarizations P_M and P_G are induced in the MNP and GR, respectively. The P_M and P_G polarizations in turn produce electric fields E_M^Q and E_G^Q at the QE. Here subscripts Q, M and G stand for the QE, MNP and GR, respectively. Hence three electric fields E_P, E_M^Q and E_G^Q are falling on the QE. Therefore, we have

$$E_T = E_P + E_M^Q + E_G^Q \tag{3.7}$$

Let us calculate the electric fields E_M^Q and E_G^Q appearing in equation (3.7) as follows.

We know that three electric fields fall on GR: (i) the probe field E_P, (ii) the dipole electric field from the QE denoted as E_Q^G, and (iii) the dipole electric field from the MNP denoted as E_M^G. Then the total electric field seen by GR is equated to $E_P + E_Q^G + E_M^G$. Similarly, the total electric falling on the MNP is equal to $E_P + E_Q^M + E_G^M$ where E_Q^M and E_G^M are the dipole electric fields produced by the QE and GR, respectively. Using the quasi-static approximation [32, 35]

the polarization P_G of the GR can be calculated as

$$P_G = \alpha_G \left(\frac{E_P + E_Q^G + E_M^G}{\epsilon_{ef}} \right) \tag{3.8}$$

$$\alpha_G = \frac{V_G \left[\epsilon_G (\omega) - \epsilon_b \right]}{3\epsilon_b + 3\varsigma_l \left[\epsilon_G (\omega) - \epsilon_b \right]} \tag{3.9}$$

where ϵ_{ef} is the effective dielectric constant and α_G is the polarizability of the GR. Similarly, we can calculate the polarization P_M of the MNP using the quasi-static approximation [32, 38] as

$$P_M = \alpha_M \left(\frac{E_P + E_Q^M + E_G^M}{\epsilon_{ef}} \right) \tag{3.10}$$

$$\alpha_M = \frac{V_M \left[\epsilon_M (\omega) - \epsilon_b \right]}{\epsilon_M (\omega) + 2\epsilon_b} \tag{3.11}$$

where α_M is the polarizability of the MNP. The $\epsilon_G(\omega)$ and $\epsilon_M(\omega)$ terms appearing in equations (9) and (11) denote the dielectric functions of the GR and MNP, respectively. Here V_M and V_G are the volume of the MNP and GR, respectively. The ς_l term is called the depolarization factor [32]. The dielectric constant of the GR has been calculated in the presence of the surface plasmon-photon couplings by using Green's function method in the random phase approximation. It is written as [32, 36]

$$\epsilon_G(\omega) = \epsilon_\infty^G - \frac{e^2}{2q\epsilon_0} \Pi_G(q, \omega) \tag{3.12}$$

$$\Pi_G(q, \omega) = \frac{2q\epsilon_0 \omega_G^2}{e^2 (\omega + i\gamma_G)^2} \tag{3.13}$$

where ϵ_∞^G is the high frequency dielectric constant of the GR, ϵ_0 is dielectric constant of vacuum, and $\Pi_G(q, \omega)$ is the 2D polarizability function. Here ω_G is called plasmon frequency of GR, q is the wave vector, e is the electron charge and γ_G is the decay rate of the GR plasmon. The

following equation for ϵ_M is used widely in the literature

$$\epsilon_M(\omega) = \epsilon_\infty^M - \omega_M^2/(\omega + i\gamma_M)^2 \tag{3.14}$$

where ϵ_∞^M is the high frequency dielectric constant, ω_M is called plasmon frequency and γ_M is the decay rate. It is interesting to note that $Re(\epsilon_M(\omega))$ and $Re(\epsilon_G(\omega))$ have negative values for certain values of ω. This means the denominators of α_G and α_M in equations (9) and (11) can become zero for certain frequencies say ω_{sp}^G and ω_{sp}^M which they are called the SPP resonance frequencies for GR and MNP, respectively.

We have found the polarization P_Q, P_G and P_M in equation (3.4), (3.8) and (3.10) for QE, GR and MNP, respectively. Now we can calculate the electric fields produced by these polarizations by using the identity [32] $E_i = g_l |\mathbf{P}_i| / 4\pi\epsilon_{ef} |\mathbf{R}|^3$ (i = P, M, G). where the constant g_l is called the polarization parameter and it has values $g_l = -1$ and $g_l = 2$ for $\mathbf{P}_i \shortparallel \mathbf{R}$ and $\mathbf{P}_i \perp \mathbf{R}$, respectively. Let the center to center distance between the QE and the MNP, QE and GR, and MNP and GR be denoted as R_{QM} and R_{QG} and R_{MG}, respectively. Putting expression of P_Q from equation (3.4) in this identity we can calculate the electric field produced by the QE at the GR (E_Q^G) and at the MNP (E_Q^M) as

$$E_Q^G = \frac{g_l \alpha_Q E_P}{4\pi\epsilon_{ef}^2 R_{QG}^3} \tag{3.15a}$$

$$E_Q^M = \frac{g_l \alpha_Q E_P}{4\pi\epsilon_{ef}^2 R_{QM}^3} \tag{3.15b}$$

Similarly, using equation (3.8) in the identity we can calculate the electric field produced by the GR at the QE (E_G^Q) and at the MNP (E_G^M) as

$$E_G^Q = \frac{g_l \alpha_G \left(E_P + E_Q^G + E_M^G\right)}{4\pi\epsilon_{ef}^2 R_{QG}^3} \tag{3.16a}$$

$$E_G^M = \frac{g_l \alpha_G \left(E_P + E_Q^G + E_M^G\right)}{4\pi\epsilon_{ef}^2 R_{MG}^3} \tag{3.16b}$$

Following the above method electric fields produced by the MNP at the QE (E_M^Q) and at the GR (E_M^G) are calculated as

$$E_M^Q = \frac{g_l \alpha_M \left(E_P + E_Q^M + E_G^M\right)}{4\pi\epsilon_{ef}^2 R_{QM}^3} \tag{3.17a}$$

$$E_M^G = \frac{g_l \alpha_M \left(E_P + E_Q^M + E_G^M\right)}{4\pi\epsilon_{ef}^2 R_{MG}^3} \tag{3.17b}$$

Solving equations (15-17) and after some mathematical manipulations we get the expressions of electric fields falling on the QE from the GR (E_G^Q) and from the MNP (E_M^Q) as

$$E_G^Q = \frac{g_l \alpha_G E_P}{4\pi\epsilon_{ef}^2 R_{QG}^3} + \frac{g_l^2 \alpha_G \alpha_Q E_P}{\left(4\pi\epsilon_{ef}^2\right)^2 R_{QG}^6} + \frac{g_l^2 \alpha_G \alpha_M E_P}{\left(4\pi\epsilon_{ef}^2\right)^2 R_{QG}^3 R_{MG}^3} \tag{3.18a}$$

$$E_M^Q = \frac{g_l \alpha_M E_P}{4\pi\epsilon_{ef}^2 R_{QM}^3} + \frac{g_l^2 \alpha_M \alpha_Q E_P}{\left(4\pi\epsilon_{ef}^2\right)^2 R_{QM}^6} + \frac{g_l^2 \alpha_M \alpha_G E_P}{\left(4\pi\epsilon_{ef}^2\right)^2 R_{QM}^3 R_{MG}^3} \tag{3.18b}$$

To get the above expression we have neglected the R^{-9} terms which are negligible compared to R^{-3} and R^{-6} terms. Note the electric field, E_G^Q, produced by the GR at the QE has three terms. The first term is the induced dipole field created by the probe field E_P and it depends on R_{QG}^{-3}. The second term is the induced dipole field produced by the QE dipole field and it decays as R_{QG}^{-6}. The last term is the indirect electric field produced by the MNP which induces a dipole in the GR which in turn induces an electric field at the QE and it depends on R_{QG}^{-3} and R_{QM}^{-3}. Similarly, the MNP electric field at the QE also has three terms which have similar physical meaning as above. It is interesting to point out that the QE not only feels the direct electric field from the MNP but also sees the indirect electric field from the MNP induced by the GR. Similarly, the QE feels the direct electric field from the GR along with the indirect electric field from GR induced by the dipole field of the MNP.

3.2.2 Density matrix method and photoluminescence

In this section we calculate PL which is defined in equation (3.1) and it depends on the radiative and nonradiative decay rates. The decay rates are calculated by using the quantum perturbation theory. The Hamiltonian of the non-interacting QE can be written as

$$H_{EX} = \hbar\omega_a\sigma_{aa} + \hbar\omega_b\sigma_{bb} \tag{3.19}$$

where $\sigma_{ii} = |i\rangle\langle i|$ with i=a,b and $\hbar\omega_a$ and $\hbar\omega_b$ are the energy of levels $|a\rangle$ and $|b\rangle$. The exciton energy is found as $\hbar\omega_{ab} = \hbar\omega_b - \hbar\omega_a$.

Therefore, the dipole μ of the QE interacts with electric field E_T falling on the QE and the interaction Hamiltonian in the dipole approximation is written as

$$H_{int} = \mu.E_T = -\mu.E_P - \mu.E_M^Q - \mu.E_G^Q \tag{3.20}$$

The last two terms are the exciton-SPPs interaction with MNP and GR, respectively. They are also called the DDI (dipole-dipole interaction) since the dipole of the QE interacts with dipoles of MNP and GR via their electric fields. Putting equations (18a, 18b) into the interaction Hamiltonian, equation (3.20) and after some mathematical manipulations in the rotating wave approximation we get

$$H_{int} = H_{e-p} + H_{DDI} \tag{3.21a}$$

$$H_{e-p} = -\Omega_P\sigma_{ab}^{\dagger} + c.c. \tag{3.21b}$$

$$H_{DDI} = -\left(\Pi_{QM} + \Lambda_{QM}\right)\sigma_{ab}^{\dagger} - \left(\Pi_{QG} + \Lambda_{QG}\right)\sigma_{ab}^{\dagger} + \left(\Phi_{QGM} + \Phi_{QGM}\right)\sigma_{ab}^{\dagger} \tag{3.21c}$$

$$\Pi_{QG} = \frac{g_l\alpha_G\Omega_P}{4\pi\epsilon_{ef}^2 R_{QG}^3}, \Lambda_{QG} = \frac{g_l^2\alpha_G\alpha_Q\Omega_P}{\left(4\pi\epsilon_{ef}^2\right)^2 R_{QG}^6}, \Phi_{QGM} = \frac{g_l^2\alpha_G\alpha_M\Omega_P}{\left(4\pi\epsilon_{ef}^2\right)^2 R_{QG}^3 R_{MG}^3} \tag{3.21d}$$

$$\Pi_{QM} = \frac{g_l\alpha_M\Omega_P}{4\pi\epsilon_{ef}^2 R_{QM}^3}, \Lambda_{QM} = \frac{g_l^2\alpha_M\alpha_Q\Omega_P}{\left(4\pi\epsilon_{ef}^2\right)^2 R_{QM}^6}, \Phi_{QMG} = \frac{g_l^2\alpha_M\alpha_G\Omega_P}{\left(4\pi\epsilon_{ef}^2\right)^2 R_{QM}^3 R_{MG}^3} \tag{3.21e}$$

where Ω_P is called the Rabi frequency and is defined as $\Omega_P = \mu_{ab} E_P / 2\hbar\epsilon_Q$ with ϵ_Q as the dielectric constant of the QE. Here μ_{ab} is the induced dipole moment due to the transition $|a\rangle \rightarrow |b\rangle$, and $\sigma_{ab}^{\dagger}$ is called the exciton raising operator for transition $|a\rangle \leftrightarrow |b\rangle$.

The first term H_{e-p} is the interaction of the QE due the probe field. The second term H_{DDI} is the exciton-SPPs coupling term. It is also called the DDI term since the SPPs induce dipoles in MNP and GR interact with exciton induced dipole in the QE. It is important to note that when the probe frequency ω is in resonance with ω_{sp}^{G} and ω_{sp}^{M} then α_G and α_M have very large values. This in turn makes the DDI very strong. This effect will be exploited in the results and discussion section. The two Π_{QM} and Π_{QG} terms are due to the interaction of the QE with the dipole electric field from the MNP and GR, respectively. The other two terms, Λ_{QM} and Λ_{QG}, are due to the interaction of the QE with a dipole field from MNP and GR, respectively, and is the self-interaction of the QE, as it depends on the polarization of the QE. The term Φ_{QGM} is the indirect interaction between the QE and the MNP via GR. Similarly, the term Φ_{QMG} is the indirect interaction between the QE and the GR via the MNP.

The excited state in the QE decays to the ground state due to the spontaneous emission. Energy is also lost due to exciton-SPPs in MNP and GR. The interaction Hamiltonian can be found in the second quantization operator notation using the rotating wave approximation as

$$H_{decay} = -\sum_{i=P,G,M,GM,MG} \sum_{k} g_{Qi}(\varepsilon_k) \left[a_k \sigma_{ab} e^{-i(\varepsilon_{ab} - \varepsilon_k)} + h.c. \right] \tag{3.22}$$

where g_{Qi} is the coupling constant and is written as

$$g_{QP}(\varepsilon_k) = i \left(\frac{\varepsilon_k \mu_{ab}^2}{2\epsilon_0 \pi V_Q} \right)^{1/2} \tag{3.23a}$$

$$g_{QM}(\varepsilon_k) = g_{QP}(\varepsilon_k) \left(\Pi_{QM} + \Lambda_{QM} \right)^{1/2} \tag{3.23b}$$

$$g_{QG}(\varepsilon_k) = g_{QP}(\varepsilon_k) \left(\Pi_{QG} + \Lambda_{QG} \right)^{1/2} \tag{3.23c}$$

$$g_{QMG}(\varepsilon_k) = g_{QP}(\varepsilon_k) \left(\Phi_{QMG} \right)^{1/2} \tag{3.22d}$$

$$g_{QGM}(\varepsilon_k) = g_{QP}(\varepsilon_k) \left(\Phi_{QGM} \right)^{1/2} \tag{3.23e}$$

where operator a_k is the photon annihilation operator for energy ε_k, and parameter σ_{ab}=$|a\rangle\langle b|$ The first term g_{QP} is the interaction of the QE due to the vacuum field, which is responsible for the spontaneous radiative decay. The other terms are exciton-SPPs interaction (DDI) terms that are responsible for the nonradiative decay. The equation of motion for the matrix elements ρ_{ab} and ρ_{bb} is found as

$$\frac{d\rho_{bb}}{dt} = -2\Gamma_{int}\rho_{bb} - i\Omega_T\rho_{ab} + i\left(\Omega_T\right)^*\rho_{ba} \tag{3.24}$$

$$\frac{d\rho_{ba}}{dt} = -(\Gamma_{int} + i\delta_{ab})\rho_{ba} - i\left(\Omega_T\right)(\rho_{bb} - \rho_{aa}) \tag{3.25}$$

where $\delta_{ab} = \omega_{ab} - \omega$ is called the detuning parameter and $\Omega_T = \mu_{ab}E_T/2\hbar\epsilon_Q$. The matrix element ρ_{aa} can be found as $\rho_{aa} = 1 - \rho_{bb}$. The decay rate Γ_{int} appearing in equation (3.24, 3.25) is found as

$$\Gamma_{int} = \frac{2\pi}{\hbar}\sum_k |\langle f|\, H_{int}\, |i\rangle|^2\, \delta(\omega_k - \omega_{ab}) \tag{3.26}$$

where the initial state $|i\rangle$ is taken such that the exciton is in the excited state $|b\rangle$ and there are no photons $|0_k\rangle$ i.e. $|i\rangle = |b, 0_k\rangle$. Similarly, the final state $|f\rangle$ is considered in such a way that an exciton is in the ground state $|a\rangle$ and there is one photon state $|1_k\rangle$ i.e. $|f\rangle = |a, 1_k\rangle$. The summation over k can be replaced by integration using the idea of the density of states $D(\omega_k)$. The decay rates can be expressed in term of $D(\omega_k)$ as

$$\Gamma_{int} = \frac{2\pi}{\hbar}\sum_{i=P,G,M,GM,MG}\int \left|g_{Qi}\left(\omega_k\right)\right|^2 D\left(\omega_k\right)\delta(\omega_k - \omega_{ab}) \tag{3.27}$$

where $D(\varepsilon_k)$ is the density of state of emitted photons and found as $D(\varepsilon_k) = V_Q\varepsilon_k^2/3\pi^2/\left(\hbar c\right)^3$. Using this equation for $D(\varepsilon_k)$ and putting equations (24, 25) into equation (3.27) we get the

expressions for the decay rates as

$$\begin{aligned} \Gamma_{int} &= \Gamma_{QP} + \Gamma_{NR}^{direct} + \Gamma_{NR}^{indirect} \\ \Gamma_{NR}^{direct} &= \Gamma_{QM} + \Gamma_{QG} \\ \Gamma_{NR}^{indirect} &= \Gamma_{QMG} + \Gamma_{QGM} \end{aligned} \tag{3.28}$$

where Γ_{NR}^{direct} is the *direct nonradiative* decay rate and contains two terms Γ_{QM} and Γ_{QG}, $\Gamma_{NR}^{indirect}$ is the *indirect nonradiative* decay rate and contains two terms Γ_{QMG} and Γ_{QGM}. They are calculated as

$$\Gamma_{QP} = \frac{\mu_{ab}^2 \varepsilon_{ab}^3}{3\pi\epsilon_0 \hbar^4 c^3} \tag{3.29a}$$

$$\Gamma_{QM} = \Gamma_{QP}\left(\Pi_{QM} + \Lambda_{QM}\right);\ \Gamma_{QG} = \Gamma_{QP}\left(\Pi_{QG} + \Lambda_{QG}\right) \tag{3.29b}$$

$$\Gamma_{QMG} = \Gamma_{QP}\left(\Phi_{QMG}\right);\ \Gamma_{QGM} = \Gamma_{QP}\left(\Phi_{QGM}\right) \tag{3.29c}$$

where ε_{ab}=$\hbar\omega_{ab}$. Here Γ_{QM} is the direct nonradiative decay rate when the exciton energy is transferred from the QE to the MNP, Γ_{QG} is the direct nonradiative decay rate when the exciton energy is transferred from the QE to the GR. On the other hand, Γ_{QMG} is the indirect nonradiative decay rate when the exciton energy is transferred from the QE to the GR via the MNP, and Γ_{QGM} is the indirect nonradiative decay rate when the exciton energy is transferred from the QE to the MNP via the GR.

Now we can evaluate the PL quantum yield given in equation (3.2). Putting equation (3.28) into equation (3.2) we get the expression of the PL quantum yields as

$$Q_{PL} = \left(\frac{1}{1 + \left(\Pi_{QM} + \Pi_{QG}\right) + \left(\Lambda_{QM} + \Lambda_{QG}\right) + \left(\Phi_{QMG} + \Phi_{QGM}\right)}\right) \tag{3.30}$$

Note that in the absence of the DDI we get $Q_{PL} = 1$.

We define the PL efficiency as E_{PL}. PL efficiency is ratio of the power emitted by the QE

in vacuum and the power emitted by the QE in the presence of the MNP and GR

$$E_{PL} = \frac{P^0_{PL}}{P_{PL}} \tag{3.31}$$

where P^0_{PL} is the power emitted by the QE due to the spontaneous emission only and it is obtained from P_{PL} by putting the DDI terms equal to zero (i.e. $H_{DDI} = 0$).

Finally, we can derive the expression of the PL (P^{QM}_{PL}) for the QE-MNP hybrids. This expression can be obtained from the PL expression of the QE-MNP-GR by putting $\alpha_G = 0$. This gives us

$$P^{QM}_{PL} = Q^{QM}_{PL} W_{QE} \tag{3.32a}$$

$$Q^{QM}_{PL} = \left(\frac{1}{1 + \Pi_{QM} + \Lambda_{QM}} \right) \tag{3.32b}$$

Similarly, we can derive the expression of the PL for the QE-GR (P^{QG}_{PL}) hybrids by putting $\alpha_M = 0$ and we get

$$P^{QG}_{PL} = Q^{QG}_{PL} W_{QE} \tag{3.33a}$$

$$Q^{QG}_{PL} = \left(\frac{1}{1 + \Pi_{QG} + \Lambda_{QG}} \right) \tag{3.33b}$$

Note that the PL does not have Φ_{QMG} and Φ_{QGM} terms. The Im(ρ_{ab}) appearing in W_{QE} will be evaluated by numerically using MAPLE subroutine in the next section.

3.3 Results and Discussion

In this section we compared our theory with the experiments of QD-GR hybrid [17] and QD-MNP-GR [18] hybrid systems. Let us first apply our theory to the QD-GR hybrid. In this experiment the PL intensity of CdTe QD is measured alone and then measured in the presence of the GR by varying the concentration of GR. Their results are plotted in Figure 3.2 as solid

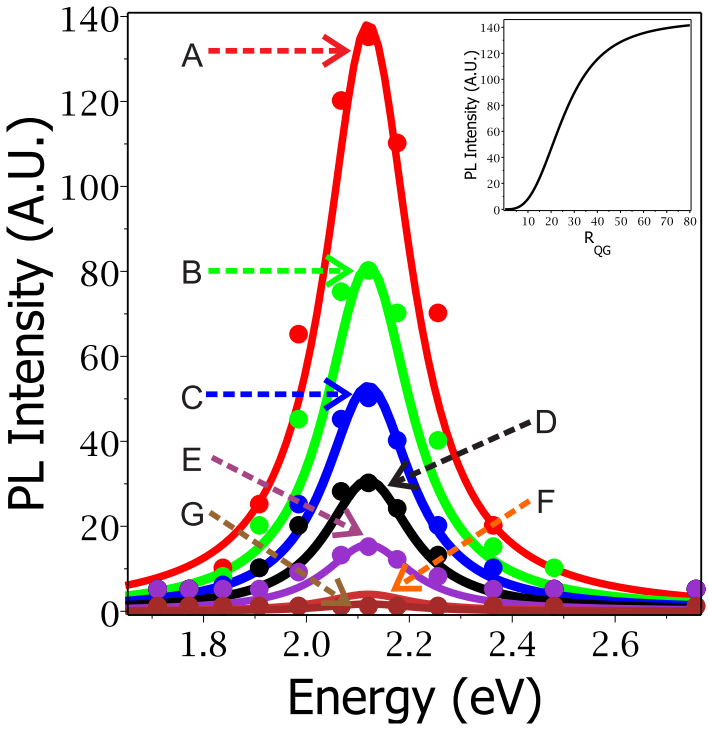

Figure 3.2: PL emission spectra of QE-GR system. The solid curves correspond to theoretical results, while the solid circular dots indicate experimental result. Curve and solid circles of A indicate QE without GR. Curves and solid circles of B-G indicate QE-GR hybrid system with GR concentrations of 0.02, 0.04, 0.06 0.08 0.10 0.012 $\mu g/mL$ and R_{QG} of 29, 22, 17, 13, 8, 6 nm.

circles. The CdTe QDs has a mean radius 3.09 nm, and the exciton resonance energy $\hbar\omega_{ab}$ = 2.30 eV. Physical parameters for the QD are taken as $\epsilon_Q = 6.25$ [37] $\Gamma_{QD} = 3.8 * 10^{-4} meV$[37], $\Omega_p = 3.9 * 10^{-3} meV$[38] and $\mu_{ab} = 0.1e \times nm$. For GR we have taken V_G =1.8 μm, $\epsilon^G_\infty = 2.00$ [39], $\omega_G = 8.60eV$ [39], and $\gamma_G = 0.008eV$ [40] which are found similar in those references. The SPP energy $\hbar\omega^G_{sp}$ for GR has been calculated using the GR polarizability (α_G) given in equation (3.9). The experimental parameter for the average thickness of the GR was about 2 nm. The SPP energy is found as $\hbar\omega^G_{sp}$ =2.29 eV which is very close to $\hbar\omega_{ab}$. This means the exciton energy is in resonance with the SPP energy ($\hbar\omega^G_{sp} \approx \hbar\omega_{ab}$). This condition makes the GR polarizability (α_G) large as can be seen from equation (9). This in turn enhances the DDI terms Π, Λ and Φ in equations (29), which means the DDI plays an important role in PL quenching.

We compare our theory with the above experimental work in Figure 3.2 where the PL intensity in arbitrary units (A.U.) is plotted as a function of energy (eV). Solid circles denoted by A indicate the PL intensity of QDs alone, while the B–G-solid circles correspond to PL intensity with GR at concentrations of 0.02, 0.04, 0.06, 0.08, 0.1, $0.12\mu g/mL$. Theoretical results are plotted by the solid curves. The A- solid curve is plotted using equation (3.33) without the DDI term. One can see that there is a good agreement with theory and experiment.

To explain the PL experiment with GR concentration we have considered that the distance between the QD and GR decreases as the concentration of GR increases. Our theoretical results are plotted in Figure 3.2 by the B-G solid curves. Note that as the concentration increases the PL quenching also increases. This is because the nonradiative energy transfer from the QD to the GR increases as the distance between the QD and GR decreases. This effect is represented by the DDI coupling seen in Π_{QG} and Λ_{QG} terms. Note that the Π_{QG} varies as R_{QG}^{-3} and Λ_{QG} depends as R_{QG}^{-6}, where the former is the dominating term. The effect of GR on the PL quenching on QE can be further seen in the Figure 3.2 inset. Here maximum PL intensity (A.U.) is plotted as a function of R_{QG}(nm). Results show that as R_{QG} changes the intensity of peaks also changes. Once R_{QG} becomes large enough the intensity of QE-GR hybrid systems resembles the intensity of free-QE.

The relation between the GR concentration (C_{GR}) and the average distance between QE and GR (R_{QG}) is plotted in Figure 3.3. Here PL intensity is taken at the peaks of the B-G curves. Note that the PL intensity decreases as the concentration increases. The solid circles are experimental data. We have found that the following expression which fits the experiment data

$$C_{GR} = A_{GR} \exp(-\alpha_{GR} R_{QG})$$

where A_{GR} and α_{GR} are fitting parameters and are found as $\alpha_{GR} = 0.075m^{-1}$ and $A_{GR} = 0.1979\mu g/mL$. The above equation is going to be very useful to find the relation between the concentration and distance between nanosystem in future experiments.

Now we study the PL quenching in a QE-MNP-GR hybrid system using experimental data

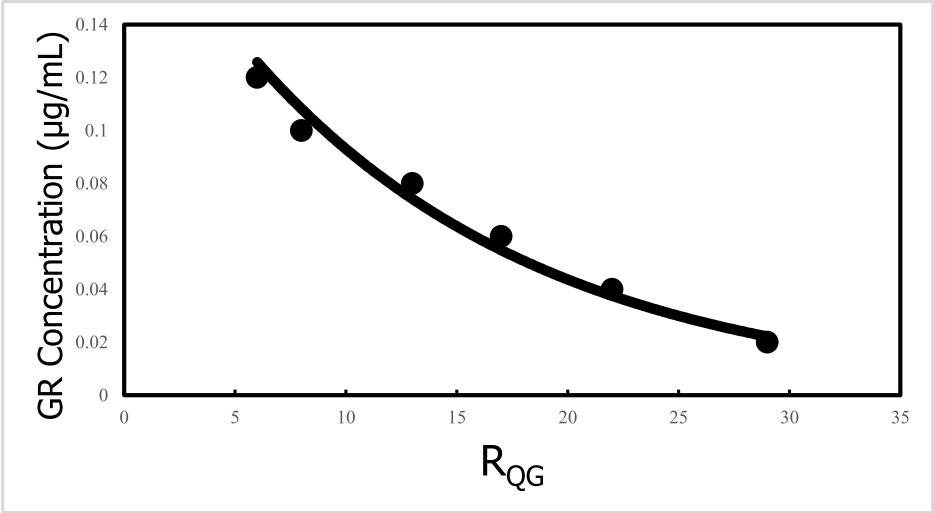

Figure 3.3: Concentration (μg/mL) of GR plotted as a function of $R_{QG}(nm)$. The solid curve represents an exponential line of best fit.

of Zeng et al. [18]. They have used CdTe QD as a QE and the MNP as gold (Au). This QD has a maximum absorption at $\hbar\omega_{ab}$ =2.36eV. The physical parameters for GR, found similar in reference, are V_G =1.8μm, $\epsilon_\infty^G = 2.40$ [39], $\omega_G = 9.01eV$ [39], and $\gamma_G = 0.08eV$ [40]. While the parameters for Au MNP are taken as V_M =125nm, $\epsilon_\infty^G = 1.80$ [41], $\omega_M = 8.75eV$ [41], and $\gamma_M = 0.001eV$ [41] similarly, found in that reference. The SPP energy $\hbar\omega_{sp}^G$ and $\hbar\omega_{sp}^M$ for the GR and Au MNP has been calculated using the polarizability α_G and α_M given in equations (9 and 11). We found $\hbar\omega_{sp}^G$ =2.37 eV and $\hbar\omega_{sp}^M$ =2.38 eV which are very close to $\hbar\omega_{ab}$. This means the exciton energy is in resonance with the SPP energies and DDI plays an important role in the PL quenching. The concentration of QDs in their experiments is taken as $0.01 \times 10^{-5} mol/L$. This gives us the distance between QDs as approximately equal to 250 nm. Which means we can neglect the DDI between QDs in our calculations. After the hybridization the distance between the GR and the QD was about R_{QG} =10nm and the distance between the MNP and the QD was about R_{QM} =10nm.

Measured PL intensity of QD alone, QD-MNP, and QD-GR-Au MNP is plotted in Figure 3-4 by A, B, and C solid circles, respectively. Their results show that with the addition of Au MNPs, PL quenching was observed. Furthermore with the addition of GR, the quenching

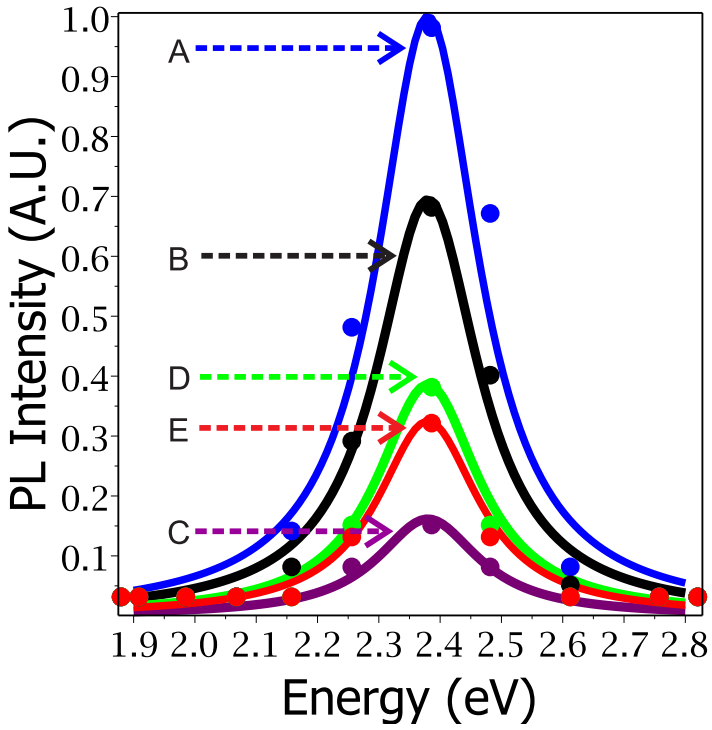

Figure 3.4: PL emission spectra of QE-MNP-GR system. The solid curves correspond to theoretical results, while the solid circular dots indicate experimental result. Curve and solid circles of A indicate QE without GR and MNP. Curves and solid circles of B indicate QE-MNP hybrid system with R_{QM} = 10nm. Curves and solid circles of C indicate QE-MNP-GR hybrid system with R_{QM} = R_{QG} =10nm and R_{MG} = 20nm. Solid circles of C and D indicate QE-MNP-GR bound with antigen concentration of 0.1ng/mL and 0.05ng/mL, respectively. Curves of C and D represent QE-MNP-GR with R_{QM} = 40nm, R_{QG} =14nm and R_{QM} = 30nm R_{QG} =13nm and R_{MG} = 20nm, respectively.

increased again. To explain curve B we used equation (3.32) along with equations (1 and 29) to analyze curve C. The theoretical results are plotted by A, B and C solid curves. A good agreement between experiments and theory is found. The PL quenching in the B curve is due to the direct nonradiative energy transfer from the QD to the MNP due to terms Π_{QM} and Λ_{QM}.

The C curve in Figure 3.4 is for QD-MNP-GR hybrid. In this case all DDI terms (i.e. Π_{QM}, Λ_{QM}, Π_{QG}, Λ_{QG}, Φ_{QMG} and Φ_{QGM}) are included in the calculation. This means that the PL quenching occurs due to the direct nonradiative energy transfer from the QD to the MNP and from the QD to GR. The PL quenching also occurs due to the *indirect nonradiative energy transfer* from QD to the MNP via GR and from QD to GR via MNP. It is interesting to note

that the direct nonradiative process depends on the polarizability of the QD (α_Q) and distance between the QD and MNP (R_{QM}) and QD and GR (R_{QG}). On the other hand, the indirect nonradiative process does not depend on α_Q and depends on R_{MG}. This means that energy can be transported from one nanosystem to the second nanosystem through a third nanosystem.

Zeng et al. [18] have also measured the PL intensity by changing the distance between nanosystems. They have achieved this by changing the antigen concentration from 0 ng/mL to 0.1 ng/mL and 0.05 ng/mL. The experimental data (solid circles) and theoretical results (solid curves) are plotted by D and E curves in Figure 3.4 for 0.1 ng/mL and 0.05 ng/mL respectively. The antigen increases the distance between QD and MNP-GR, resulting in a recovery in the PL intensity. This is because the direct and indirect nonradiative energy transfer rates decrease as the distance between the systems reduces. Hence PL quenching decreases as the concentration of the antigen increases.

To observe the importance of the indirect nonradiative energy transfer we have plotted decay rate defined as equation (3.28) as a function of R_{MG} and kept $R_{QG} = R_{QM} = 10nm$, in Figure 3.5. Note that R_{QM}, R_{QG} and R_{MG} are related by the following equation in a triangle

$$R_{MG} = \sqrt{R_{QM}^2 + R_{QM}^2 + R_{QM}^2 R_{QM}^2 \cos\phi}$$

where ϕ is the angle between sides R_{QM} and R_{QG}. Note that by changing ϕ one can modify R_{MG} without affecting the values of R_{QM} and R_{QG}. The solid curve represents the PL efficiency E_{PL}^0 without the indirect nonradiative terms (i.e. Φ_{QMG}= Φ_{QGM} = 0) and dotted curve is the PL efficiency E_{PL} with the indirect nonradiative terms. Note that the E_{PL} increases with decreasing R_{MG} whereas E_{PL}^0 does not change. This means that we can increase the indirect nonradiative process by decreasing R_{MG} and without changing the direct nonradiative contribution. It is interesting to see that the direct radiative process falls faster than that of the indirect nonradiative process. These are interesting findings of the papers.

Finally, we study the time dependence of two indirect nonradiative energy transfer pro-

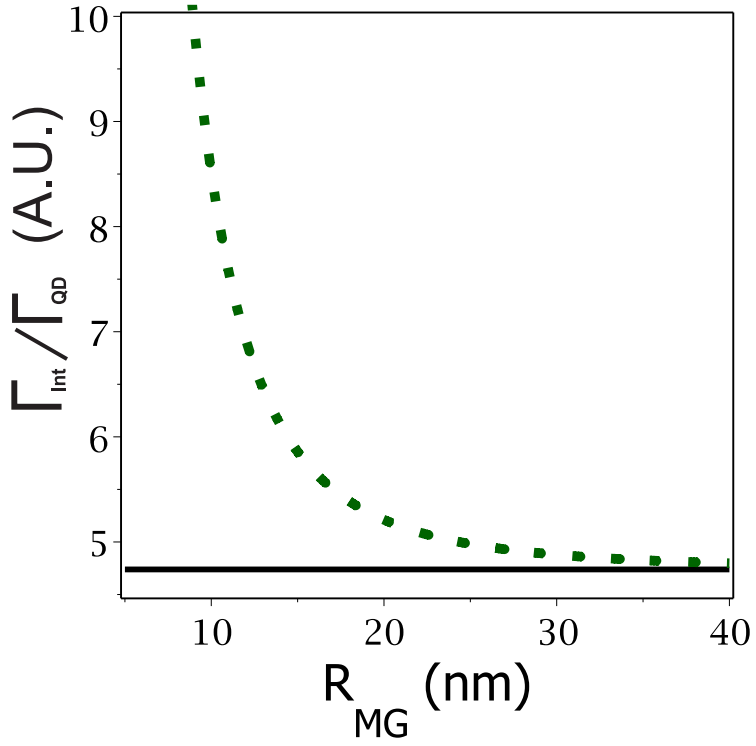

Figure 3.5: Normalized decay rate (A.U.) is plotted as a function of $R_{MG}(nm)$. The solid line corresponds to the PL efficiency without indirect nonradiative term, while the dotted curve corresponds to the PL efficiency with the indirect nonradiative term. Here, $R_{QM} = R_{QG}$ =10nm.

cesses. Note that the expression of the energy transfer rate (see equations (5) and (6)) depends on the $\mathrm{Im}\,\rho_{ab}$. Hence $\mathrm{Im}\,\rho_{ab}$ is calculated as a function of normalized time ($\tau = \Gamma_N t/\hbar$) using equations (24, 25) self consistently and only considering Φ_{QMG} and Φ_{QGM} terms. The results are plotted in Figure 3.6. The solid curve is plotted when only Φ_{QMG} is present and the rest of the terms are absent. Similarly, the dotted curve is plotted when only Φ_{QGM} is present and the rest of the terms are absent. Note that both processes starts at the same time but Φ_{QMG} increases faster and reached at highest value at $\tau = 2$, or t = 0.03ns ($\Gamma_N = 3.39 * 10^{-2} meV$). For this process the steady state reaches at $\tau = 19$ (t = 0.37ns). On the other hand the Φ_{QGM} term increases slower and reaches maximum value at $\tau = 2$ (t = 0.03ns). In this case the steady state reaches at $\tau = 15$ (t = 0.29ns). Note the Φ_{QMG} term is stronger than the Φ_{QGM} term, because GR polarizability (α_G) is larger than MNP polarizability (α_M) which decreases Γ_{int}.

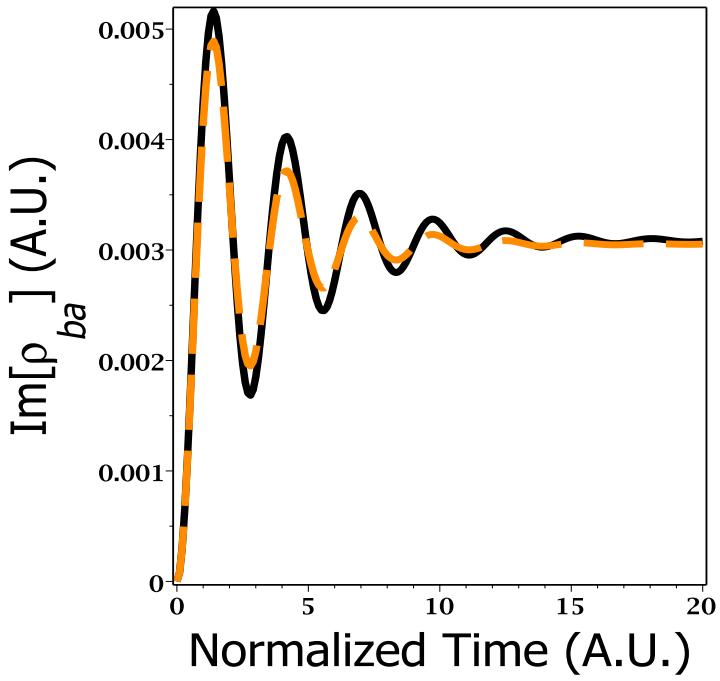

Figure 3.6: Plot of the Im ρ_{ba} as a function of normalized time, $\tau = \Gamma_N t/\hbar$. The solid curve represents when only Φ_{QMG} is present and the rest of the terms are absent, with $R_{QG} = 15nm$ and $R_{QM} = 10nm$.The dotted curve corresponds when only Φ_{QGM} is present and the rest of terms are absent, with $R_{QG} = 10nm$ and $R_{QM} = 15nm$.The other parameters are $R_{MG} = 10nm$, and $\hbar\omega$ =2.18eV.

3.4 Conclusions

In this paper a theory for PL quenching for hybrid systems made from three nanosystems such as QE, MNP and GR is developed. The quantum density matrix method and Maxwell's equations in the quasi-static approximation have been used to calculate the DDI between the nanosystems. We used the second quantized method and quantum Golden rule to calculate the radiative and nonradiative decay processes in the presence of DDI. We compared our theory with PL experiments of QD-GR hybrid [17] and QD-MNP-GR hybrid [18]. A good agreement between theory and experiments is achieved. It is found that the PL quenching in QD-MNP-GR hybrid occurs not only due the direct nonradiative energy transfer but also through the indirect nonradiative energy transfer process. It is found that the indirect nonradiative process in the QD depends on the distance between the GR and MNP.

Bibliography

[1] N. Varghese, U. Mogera, A. Govindaraj, A. Das, P.K. Maiti, A.K. Sood, and C.N.R. Rao, ChemPhysChem 10, 206 (2009).

[2] C.H. Lu, H.H. Yang, C.L. Zhu, X. Chen, and G.N. Chen, Angew. Chemie - Int. Ed. 48, 4785 (2009).

[3] J.D. Cox, M.R. Singh, G. Gumbs, M.A. Anton, and F. Carreno, Phys. Rev. B - Condens. Matter Mater. Phys. 86, (2012).

[4] R.D. Artuso and G.W. Bryant, Phys. Rev. B - Condens. Matter Mater. Phys. 82, (2010).

[5] S.M. Sadeghi, L. Deng, X. Li, and W.-P. Huang, Nanotechnology 20, 365401 (2009).

[6] S.G. Kosionis, A.F. Terzis, V. Yannopapas, and E. Paspalakis, J. Phys. Chem. C 116, 23663 (2012).

[7] Y.H. Chan, J. Chen, Q. Liu, S.E. Wark, D.H. Son, and J.D. Batteas, Anal. Chem. 82, 3671 (2010).

[8] E. Oh, M.-Y. Hong, D. Lee, S.-H. Nam, H.C. Yoon, and H.-S. Kim, J. Am. Chem. Soc. 127, 3270 (2005).

[9] H. Wu, J. Liang, and H. Han, Microchim. Acta 161, 81 (2008).

[10] M. Li, X. Zhou, S. Guo, and N. Wu, Biosens. Bioelectron. 43, 69 (2013).

[11] Y. Matsumoto, R. Kanemoto, T. Itoh, S. Nakanishi, M. Ishikawa, and V. Biju, J. Phys. Chem. C 112, 1345 (2008).

[12] T. Pons, I.L. Medintz, K.E. Sapsford, S. Higashiya, A.F. Grimes, D.S. English, and H. Mattoussi, Nano Lett. 7, 3157 (2007).

[13] X. Wu, H. Liu, J. Liu, K.N. Haley, J.A. Treadway, J.P. Larson, N. Ge, F. Peale, and M.P. Bruchez, Nat. Biotechnol. 21, 41 (2003).

[14] A. Samanta, Y. Zhou, S. Zou, H. Yan, Y. Liu, P. Long, and R. Spectroscopic, Nano Lett. (2014).

[15] A. Kasry, A.A. Ardakani, G.S. Tulevski, B. Menges, M. Copel, and L. Vyklicky, J. Phys. Chem. C 116, 2858 (2012).

[16] Y. Wen, F. Xing, S. He, S. Song, L. Wang, Y. Long, D. Li, and C. Fan, Chem. Commun. (Camb). 46, 2596 (2010).

[17] H. Dong, W. Gao, F. Yan, H. Ji, and H. Ju, Anal. Chem. 82, 5511 (2010).

[18] X. Zeng, S. Ma, J. Bao, W. Tu, and Z. Dai, Anal. Chem. 85, 11720 (2013).

[19] C.H. Lui, K.F. Mak, J. Shan, and T.F. Heinz, Phys. Rev. Lett. 105 (2010)

[20] R. Freeman, X. Liu, and I. Willner, J. Am. Chem. Soc. 133, 11597 (2011).

[21] Y. Liu, W.Q. Loh, A. Ananthanarayanan, C. Yang, P. Chen, and C. Xu, RSC Adv. 4, 35673 (2014).

[22] J.H. Jung, D.S. Cheon, F. Liu, K.B. Lee, and T.S. Seo, Angew. Chemie - Int. Ed. 49, 5708 (2010).

[23] L. Fan, Y. Hu, X. Wang, L. Zhang, F. Li, D. Han, Z. Li, Q. Zhang, Z. Wang, and L. Niu, Talanta 101, 192 (2012).

[24] Z. Liu, P. Yin, H. Gong, P. Li, X. Wang, and Y. He, J. Lumin. 132, 2484 (2012).

[25] M. Noh, T. Kim, H. Lee, C.K. Kim, S.W. Joo, and K. Lee, Colloids Surfaces A Physicochem. Eng. Asp. 359, 39 (2010).

[26] I.-S. Liu, H.-H. Lo, C.-T. Chien, Y.-Y. Lin, C.-W. Chen, Y.-F. Chen, W.-F. Su, and S.-C. Liou, J. Mater. Chem. 18, 675 (2008).

[27] L. Li, G. Wu, T. Hong, Z. Yin, D. Sun, E.S. Abdel-Halim, and J.J. Zhu, ACS Appl. Mater. Interfaces 6, 2858 (2014).

[28] Y. Li, Y. Hu, Y. Zhao, G. Shi, L. Deng, Y. Hou, and L. Qu, Adv. Mater. 23, 776 (2011).

[29] D. Pan, J. Zhang, Z. Li, and M. Wu, Adv. Mater. 22, 734 (2010).

[30] G. Eda, Y.Y. Lin, C. Mattevi, H. Yamaguchi, H.A. Chen, I.S. Chen, C.W. Chen, and M. Chhowalla, Adv. Mater. 22, 505 (2010).

[31] F. Bonaccorso, Z. Sun, T. Hasan, and a. C. Ferrari, 4, 611 (2010).

[32] D. Sarid and W. Challener, Modern Introduction to Surface Plasmons: Theory, Mathematica Modeling, and Applications (Cambridge Univeristy Press, New York, 2010).

[33] E. Le Ru and P.G. Etchegoin, Principles of Surface-Enhanced Raman Spectroscopy (Elsevier Science, Philadelphia, 2008).

[34] L. Novotny and B. Hecht, Principles of Nano-Optics, 2nd Editio (Cambridge University Press, Cambridge University Press, 2006).

[35] M.R. Singh, Electronic, Photonic, Polaritonic, and Plasmonic Materials (Wiley Customs, Toronto, 2014).

[36] E.H. Hwang and S. Das Sarma, Phys. Rev. B - Condens. Matter Mater. Phys. 75, (2007).

[37] I. Hemdana, M. Mahdouani, and R. Bourguiga, Phys. B Condens. Matter 407, 3313 (2012).

[38] J.R. Schaibley, a P. Burgers, G. a McCracken, D.G. Steel, a S. Bracker, D. Gammon, and L.J. Sham, Phys. Rev. B 87, 115311 (2013).

[39] T.J. Constant, S.M. Hornett, D.E. Chang, and E. Hendry, Nat. Phys. 12, 124 (2015).

[40] A. Politano and G. Chiarello, Nanoscale 6, 10927 (2014).

[41] P.G. Etchegoin, E.C. Le Ru, and M. Meyer, J. Chem. Phys. 125, 164705 (2006).

Chapter 4

Photoluminescence quenching theory in metamaterial, quantum dots and metallic nanoparticles hybrid systems including local fields

In the last section, photoluminescence quenching was observed in a system of quantum dots with graphene and metallic nanoparticles. Photoluminescence was quenched due to the interaction between excitons in the semiconductor quantum dot with the surface plasmon polaritons energies. In this chapter we study optical properties in a system composed of quantum dots with metamaterials and metallic nanoparticles. Photoluminescence quenching of the quantum dots will be investigated when they are in the vicinity of metamaterials and gold metallic nanoparticles.

4.1 Introduction

Nanoscale research in new artificial materials have had great interests due to the numerous optical properties these systems hold. Research in metamaterials, which are classified as artificial materials, have shown great importance due to its applications in superlenses, medical sensing, and telecommunication [1-7]. Large areas of metamaterial research involve exploiting the zero and negative index of refraction feasibility. Recently, researchers have fabricated an on-chip integrated metamaterial with a refractive index of zero in the optical regime, which is applicable in integrated optics [1]. Compared to noble metals and other system, such as graphene and quantum dots (QDs), metamaterials have seen much fewer theoretical and experimental work [10-20].

Metamaterials, similar to noble metals, have the ability to form surface plasmon polaritons (SPPs), thus allowing a variety of optoelectronic properties in hybrid systems, such as photoluminescence (PL). Recently, groups have started focusing on PL properties in metamaterial systems, because of the exotic properties metamaterials possess [21-24]. Metamaterials alone possess the possibility for PL research, however, for more tunable system, metamaterial hybrids systems have also been researched.

Here, we study PL quenching from QDs doped in a dielectric substrate, metamaterial, and metallic nanoparticle hybrid system. Our aim is to develop theory for PL quenching in this metamaterial hybrid system influenced both SPP field and local field. QDs can be interchanged with any quantum emitter, such as chemical and biological dyes. A schematic diagram of the nano-hybrid system is shown in Figure 4.1A. The metamaterial we consider contains a unit cell of a split-ring resonator and a metallic rod which we will denote as SRM. We also consider gold nanoparticles, AuNP, and PbS QDs denoted as MNP and QD, respectively. Two SPPs are formed at the interfaces of the dielectric slab with the SRM and the MNP. These two SPPs interact with the excitons in the QD via the excition-SPPs interaction, sometimes called dipole-dipole interaction, which has been evaluated in the rotating wave approximation. Using the many body quantum theory called the density matrix method we calculate the PL intensity

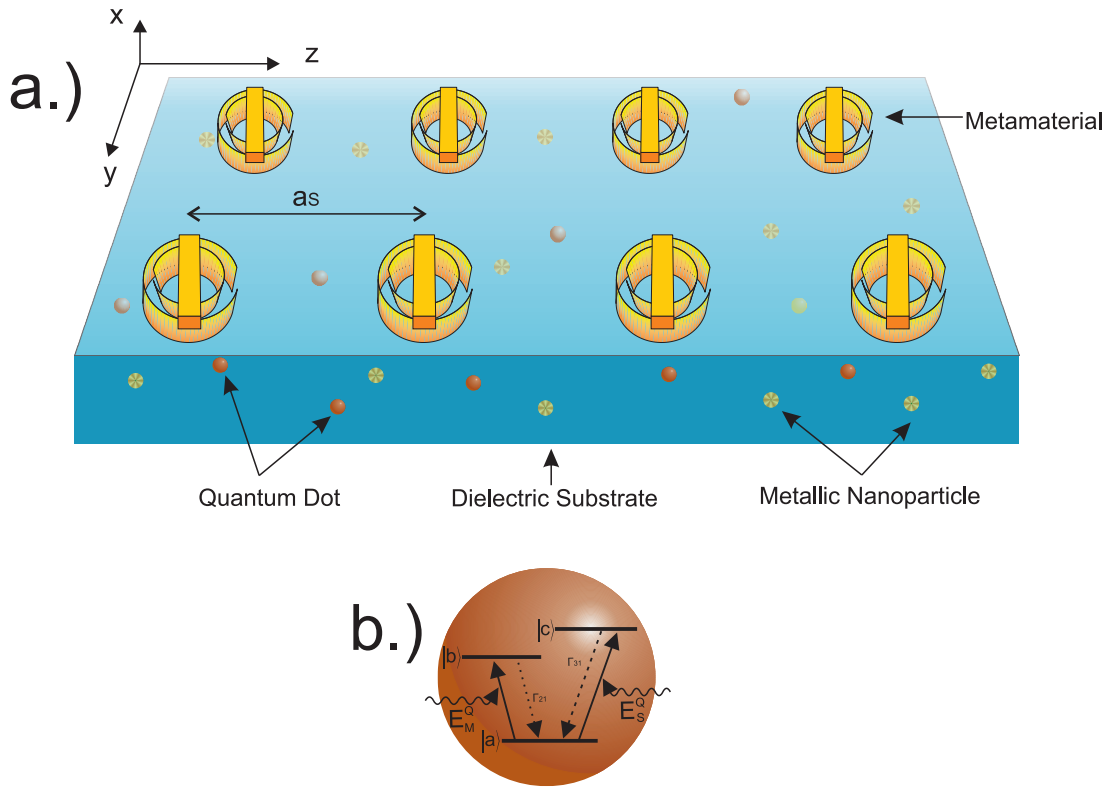

Figure 4.1: a) A schematic diagram of SRM-MNP-QD hybrid system deposited on a dielectric substrate. b) A schematic diagram of a QD with three energy levels in a V-configuration. Level |a⟩ indicates the ground level while levels |b⟩ and |c⟩ corresponds to two excited states. Metamaterial's SPP couples with transition |a⟩ - |b⟩ of the QD while MNP's SPP couples with transition |a⟩ - |c⟩.

for QDs and the radiative and nonradiative decay processes in the presence of the excition-SPPs interaction. Maxwell equations in quasi-static approximation [25] was used to calculate the fields of the system. Our results provide interesting findings that can be used to fabricate nanosenors and other optoelectronic devices for various fields.

4.2 Theoretical Formalism

4.2.1 Photoluminescence quenching

The objective of this paper is to study PL quenching of doped QDs within a SRM-MNP dielectric substrate hybrid system, seen in Figure 4.1A. Our SRM is a split-ring resonator and

metallic rod metamaterial placed on top of a dielectric substrate, in which MNP and QD are located near the interface. SPPs form at the interface between the SRM and MNP with the dielectric substrate, when an external field is applied to the system. Here we consider a QD with three discrete electronic states, one ground state $|a\rangle$, and two excited states $|b\rangle$ and $|c\rangle$. A schematic diagram of the QD is shown in Figure 4.1B. We have tuned the QD in such a way that the transitions between $|a\rangle \leftrightarrow |b\rangle$ and $|a\rangle \leftrightarrow |c\rangle$ are matched with the SPP resonance energies of SRM and MNP, respectively. Finally, we have considered that the segments that make up our hybrid system are few and apart from another segments of the same type, which prevents additional interference.

PL in the QD in vacuum is a photon emitted due to a decay of energy of exciton from the excited state $|b\rangle$, or $|c\rangle$ to the ground state $|a\rangle$. This decay rate is known as the radiative decay caused by spontaneous process. It is denoted by Γ_{qd}. However, in the presence of the MNP and SRM, part of the energy rate is transferred from the QD to the MNP and SRM. This is called the non radiative process which is due to the dipole-dipole interaction between the exciton in the QD and the SPPs in MNP and SRM. This decreasing phenomena is known as quenching. The non-radiative decay rate of excitons from QD to the MNP is denoted as $\Gamma_{qd\to m}$. Similarly, the non-radiative decay rate of excitons from QD to the SRM is denoted as $\Gamma_{qd\to N}$. Hence PL quenching factor, seen in the previous chapter, is defined as

$$Q_{PL} = \left(\frac{\Gamma_{qd}}{\Gamma_{qd} + \Gamma_{qd\to M} + \Gamma_{qd\to S}} \right) \tag{4.1}$$

The PL spectrum of the QD can be analyzed from the PL efficiency by using the fluorescence quenching data which was analyzed by the following expression [26]

$$P_{PL} = Q_{PL} W_{PL} \tag{4.2}$$

where W_{PL} is the power emitted given in equation (3.3); however, in the presence of the MNP

and SRM [27]. Using the same method as in chapter 3 we are left with.

$$W_{PL} = \frac{\omega_{ab}}{2} \operatorname{Im}(\alpha_Q) \left| E_T^Q \right|^2, \tag{4.3}$$

Here α_Q represents the polarizability of the QD as seen in equation (4.5). Solving the system's fields will be calculated in the next section. Evaluating the density matrix elements, necessary for polarizability, will occur in Section 4.2.3.

4.2.2 System Fields Contribution of metallic nanoparticles and metamaterial

In this next section we calculate the total electric field E_{QD}^T upon the QD. The probe field induces polarizations P_M and P_S in the MNP and SRM, respectively. We denote subscripts Q, M, and S for QD, MNP and SRM. Therefore, in our hybrid system the QD experiences electric fields from the probe field, MNP SPP, and SRM SPP. This gives us

$$E_T^Q = E_P + E_M^Q + E_S^Q \tag{4.4}$$

A similar expression is found in equation (3.7), however in this chapter our third system is SRM and not GR. Now, first we calculate the electric fields of E_M^Q and E_S^Q seen above.

Considering the MNP, we know that three sources apply an electric field to that part of the system. The first electric field we consider is due to the probe laser. The second source is contributed from dipole electric field from the QD-excitons with MNP-SPPs. The last sources comes from the dipole electric field between SRM-SPPs with MNP-SPPs. Hence the total electric field on the MNP can be represented as

$$E_T^M = E_P + E_Q^M + E_S^M \tag{4.5}$$

Using the quasi-static approximation [25,29] the polarization of P_M of the MNP can be found

in equation (3.10)

$$P_M = \frac{\alpha_M \left(E_P + E_Q^M + E_S^M\right)}{\epsilon_{am}} \tag{4.6}$$

where ϵ_{am} is the effective dielectric constant of MNP with its environment. Here α_M is the polarizability of MNPs found in equation (3.11).

$$\alpha_M = \frac{V_M \left[\epsilon_M(\omega) - \epsilon_b\right]}{3\epsilon_b - 3\zeta \left[\epsilon_M(\omega) - \epsilon_b\right]} \tag{4.7}$$

where V_M is the volume of the MNP, ζ is called the depolarization factor and ϵ_b is the dielectric constant of the surroundings. Here, $\epsilon_M = \epsilon_\infty^M - \omega_M^2/\left(\omega + i\gamma_M\right)^2$ is the dielectric function of the MNP, where ϵ_∞^M is the high frequency dielectric constant, ω_M is called plasmon frequency, and γ_M is the decay rate.

Since we determined MNP's polarization we can calculate the electric fields produce by MNP's polarization. From referencing, the electric field produced by the QD at the MNP as [25]

$$E_M^Q = \frac{g_l \alpha_M \left(E_P + E_Q^M + E_S^M\right)}{4\pi\epsilon_{am}^2 R_{QM}^3} \tag{4.8}$$

where

$$E_Q^M = \frac{g_l \alpha_Q \left(E_P + E_M^Q + E_S^Q\right)}{4\pi\epsilon_{am}^2 R_{QM}^3}, \qquad E_S^M = \frac{g_l \alpha_S \left(E_P + E_Q^S + E_M^S\right)}{4\pi\epsilon_{as}^2 R_{SM}^3} \tag{4.9}$$

Here parameters R_{QM} and R_{SM} represent the distance between the QD with the MNP and the SRM with the MNP, respectively. Parameter g_l is called the polarization parameter and it has values of $g_l = -1$ and $g_l = 2$ when polarization is parallel and perpendicular, respectively, with the dipole's distance vector. Also parameters α_S and ϵ_{as} are SRM's polarizability and the effective dielectric constant of SRM with its environment.

Next we calculate the total electric field applied to SRM. Similarly, as the MNP, three electric fields affect the SRM: probe field, dipole electric field from the QD-excitons with

SRM-SPPs, and dipole electric field from the MNP-SPPs with SRM-SPPs.

$$E_T^S = E_P + E_Q^S + E_M^S \tag{4.10}$$

where

$$E_S^Q = \frac{g_l \alpha_S \left(E_P + E_Q^S + E_M^S\right)}{4\pi\epsilon_{as}^2 R_{QS}^3} \tag{4.11}$$

and

$$E_Q^S = \frac{g_l \alpha_Q \left(E_P + E_S^Q + E_M^Q\right)}{4\pi\epsilon_{as}^2 R_{QS}^3}, \qquad E_M^S = \frac{g_l \alpha_S \left(E_P + E_Q^M + E_S^M\right)}{4\pi\epsilon_{am}^2 R_{SM}^3} \tag{4.12}$$

here R_{QS} is the distance between the QD and the SRM. Solving equations (4.5 - 4.12) and excluding all the distances to the ninth power we get the following

$$E_M^Q = \frac{g_l \alpha_M E_P}{4\pi\epsilon_{am}^2 R_{QM}^3} + \frac{g_l^2 \alpha_M \alpha_Q E_P}{\left(4\pi\epsilon_{am}^2\right)^2 R_{QM}^6} + \frac{g_l^2 \alpha_M \alpha_S E_P}{(4\pi)^2 \epsilon_{am}^2 \epsilon_{as}^2 R_{QM}^3 R_{SM}^3} \tag{4.13}$$

$$E_S^Q = \frac{g_l \alpha_S E_P}{4\pi\epsilon_{as}^2 R_{QS}^3} + \frac{g_l^2 \alpha_S \alpha_Q E_P}{\left(4\pi\epsilon_{as}^2\right)^2 R_{QS}^6} + \frac{g_l^2 \alpha_S \alpha_M E_P}{(4\pi)^2 \epsilon_{as}^2 \epsilon_{am}^2 R_{QS}^3 R_{SM}^3} \tag{4.14}$$

We neglected the ninth power distance terms since they are negligible compared to distance to the third and sixth power. Both E_M^Q and E_S^Q have three terms. The first terms are the induced dipole field create by the probe field and it depends on the distances R_{QM}^3 and R_{QS}^3. The second terms are the induced dipole field produced by the QD dipole field and depends on distances R_{QM}^6 and R_{QS}^6. The final terms are the indirect dipole fields produced by the MNP and SRP via the QD which depends on R_{QM}^3 and R_{SM}^3, and R_{QS}^3 and R_{SM}^3.

Lastly, we calculate the polarizability of the SRM. Using transmission line theory metamaterials can be expressed as left and right handed inductors and capacitors, seen in Figure 4.1B. Thus, we get for the SRM [24, 28]

$$\alpha_S = \frac{4\pi A_i \epsilon_{am}^2 R_{QS}^3}{g_l} e^{\left(-\sqrt{Z^2 - \frac{\epsilon_d \mu_d \epsilon^2}{\hbar^2 c^2}} R_{QS}\right)} = \frac{4\pi A_i \epsilon_{am}^2 R_{QS}^3}{g_l} e^F \tag{4.15}$$

where

$$A_i = \frac{\mu_s Re\left(\sqrt{Z^2 - \frac{\epsilon_d \mu_d \epsilon^2}{\hbar^2 c^2}}\right) - \mu_d Re\left(\frac{2}{a_s} sin^{-1}\left[\frac{\epsilon^2 - \epsilon_p^2}{2\epsilon_r}\right]\right)}{\mu_s Re\left(\sqrt{Z^2 - \frac{\epsilon_d \mu_d \epsilon^2}{\hbar^2 c^2}}\right) + \mu_d R\left(\frac{2}{a_s} sin^{-1}\left[\frac{\epsilon^2 - \epsilon_p^2}{2\epsilon_r}\right]\right)} \tag{4.16}$$

$$Z = \frac{\mu_s^2\left(\frac{\sqrt{\epsilon_d \mu_d}\epsilon}{\hbar c}\right) - \mu_d^2\left(\frac{2}{a_s} sin^{-1}\left[\frac{\epsilon^2 - \epsilon_p^2}{2\epsilon_r}\right]\right)}{(\mu_s + \mu_d)(\mu_s - \mu_d)} \tag{4.17}$$

Here $\epsilon_p = \hbar/\sqrt{L_r C_l}$, and $\epsilon_r = \hbar/\sqrt{L_r C_r}$, where L_l and L_r and C_l and C_r are left and right handed inductors and capacitors, respectively. The magnetic permeability for SRM is found as $\mu_s = L_r[1 - \epsilon_p/\epsilon^2 + i\epsilon\gamma_s]/(a_m\mu_o)$, where a_m is the lattice constant and γ_s is the decay rate of SRM. Also, parameter ϵ_d and μ_d are the permittivity and permeability of the dielectric substrate, respectively.

Finally, after modifying equations (4.13-4.14) with (4.15-4.17) and $\eta_{qd} = \alpha_Q/R_{QS}^3$ we get the following

$$E_M^Q = \frac{g_l \alpha_M E_P}{4\pi\epsilon_{am}^2 R_{QM}^3} + \frac{g_l^2 \alpha_M \alpha_Q E_P}{(4\pi\epsilon_{am}^2)^2 R_{QM}^6} + \frac{g_l A_i e^F R_{SM}^3 \alpha_M E_P}{\pi\epsilon_{am}^2 R_{QM}^3 R_{SM}^3} \tag{4.18}$$

$$E_S^Q = A_i e^F E_P + A_i e^F \eta_{qd} E_P + \frac{g_l A_i e^F \alpha_M E_P}{4\pi\epsilon_{am}^2 R_{SM}^3} \tag{4.19}$$

4.2.3 Density Matrix Equation and Quenching Factor

The interaction Hamiltonian for the QD in the dipole and rotating wave approximation is written in the interaction representation as

$$H_{int} = -(\mu_{ab}\sigma_{ba} + \mu_{ac}\sigma_{ca})\left(E_p + E_S^Q + E_M^Q\right) + h.c. \tag{4.20}$$

where $\sigma_{ii} = |i\rangle\langle i|$, μ_{ii} is the dipole moment, and h.c. is the hermitian conjugate. Putting equations (4.18-4.19) with equation (4.20) we get the following

$$H_{int} = (\Omega_b + \Pi_b + \Lambda_b + \Phi_b + \alpha_b\rho_{21} + \beta\rho_{31})\,\sigma_{ba} + (\Omega_c + \Pi_c + \Lambda_c + \Phi_c + \alpha_c\rho_{31} + \beta\rho_{21})\,\sigma_{ca} \tag{4.21}$$

where

$$\Omega_b = \frac{p_{ab}E_p}{2\hbar\epsilon_d}, \quad \Pi_b = A_i e^F \Omega_b, \quad \Lambda_b = A_i e^F \eta_{qd}\Omega_b \quad , \Phi_b = \frac{g_l A_i e^F \alpha_M \Omega_b}{4\pi\epsilon_{am}^2 R_{SM}^3} \tag{4.22}$$

$$\Omega_c = \frac{p_{ac}E_p}{2\hbar\epsilon_d}, \quad \Pi_c = \frac{g_l\alpha_M\Omega_c}{4\pi\epsilon_{am}^2 R_{QM}^3}, \quad \Lambda_c = \frac{g_l^2\alpha_M\alpha_Q\Omega_c}{(4\pi\epsilon_{am}^2)^2 R_{QM}^6}, \quad \Phi_c = \frac{g_l A_i e^F R_{SM}^3 \alpha_M \Omega_c}{\pi\epsilon_{am}^2 R_{QM}^3 R_{SM}^3} \tag{4.23}$$

$$\alpha_b = \Lambda_b\Phi_b, \quad \alpha_c = \Lambda_c\Phi_c, \quad \beta = \sqrt{\alpha_b\alpha_c} \tag{4.24}$$

here α_b, α_b, and β are called the *local fields*. Using equation (4.21) and the density matrix method, the three level density matrix elements ρ_{ij} are

$$\frac{d\rho_{cc}}{dt} = -\Gamma_{31}\rho_{cc} + iX_c\rho_{ac} - iX_c^*\rho_{ca} + i\beta\left(\rho_{ba}\rho_{ac} - \rho_{ab}\rho_{ca}\right) \tag{4.25}$$

$$\frac{d\rho_{bb}}{dt} = -\Gamma_{21}\rho_{bb} + iX_b\rho_{ab} - iX_b^*\rho_{ba} + i\beta\left(\rho_{ab}\rho_{ca} - \rho_{ba}\rho_{ac}\right) \tag{4.26}$$

$$\frac{d\rho_{ca}}{dt} = -\left[F_{ca} + i\alpha_c\left(\rho_{cc} - \rho_{aa}\right) + i\beta\rho_{cb}\right]\rho_{ca} - iX_c\left(\rho_{cc} - \rho_{aa}\right) - iX_b\rho_{bc} \tag{4.27}$$

$$\frac{d\rho_{ba}}{dt} = -\left[F_{ba} + i\alpha_b\left(\rho_{aa} - \rho_{aa}\right) + i\beta\rho_{bc}\right]\rho_{ba} - iX_b\left(\rho_{bb} - \rho_{aa}\right) - iX_c\rho_{cb} \tag{4.28}$$

$$\frac{d\rho_{cb}}{dt} = -F_{cb}\rho_{cb} + iX_c\rho_{ab} - iX_b^*\rho_{ca} + i\left(\alpha_c - \alpha_b\right)\rho_{ca}\rho_{ba} + i\beta\left(|\rho_{ba}|^2 - |\rho_{ca}|^2\right) \tag{4.29}$$

Here $X_b = \Omega_b + \Pi_b + \Lambda_b + \Phi_b$ and $X_c = \Omega_c + \Pi_c + \Lambda_c + \Phi_c$. Also, $F_{ca} = i(\epsilon - \epsilon_{MNP}) + \Gamma_{31}$, $F_{ba} = i(\epsilon - \epsilon_{SRP}) + \Gamma_{21}$, and $F_{cb} = i(\epsilon_{MNP} - \epsilon_{SRP}) + \Gamma_{31} + \Gamma_{21}$. Parameter ϵ_{MNP} is the MNP-SPP resonance frequency, similarly, ϵ_{SRM} represents SRM-SPP resonance frequency. In the above expressions, Γ_{31} and Γ_{21} correspond to $\Gamma_{qd\to M}$ and $\Gamma_{qd\to S}$, respectively, and are calculated in the previous chapter

$$\Gamma_{31} = \Gamma_{qd}\left[\Pi_c + \Lambda_c + \Phi_c\right] \tag{4.30}$$

$$\Gamma_{21} = \Gamma_{qd}\left[\Pi_b + \Lambda_b + \Phi_b\right] \tag{4.31}$$

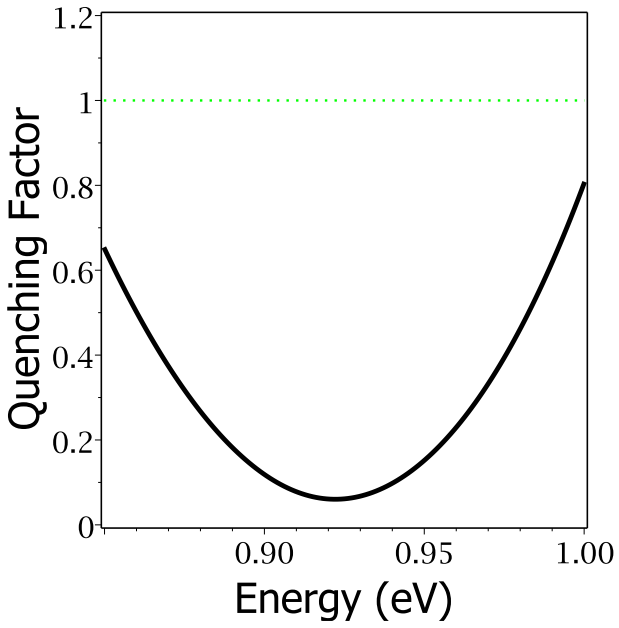

Figure 4.2: Quenching factor for a QD. Solid curve corresponds quenching without SRM-MNP, while the dashed curve corresponds to a system with SRM-MNP where all segments are 10nm apart.

Now we can calculate the PL quenching factor seen in equation (4.1). Putting equations (4.30-4.31) into equation (4.1) we get

$$Q_{PL} = \left(\frac{1}{1 + \Pi_c + \Lambda_c + \Phi_c + \Pi_b + \Lambda_b + \Phi_b} \right) \tag{4.32}$$

Notice that the PL intensity is dependent on the field contributions from the MNP and SRP. Also, note that in the absence of MNP and SRP $Q_{PL} = 1$. We solved the density matrix solutions numerically by using MAPLE software package using a DVERK78 subroutine.

4.3 Results and Discussions

In this section we evaluate the PL spectrum for the QD-MNP-SRM hybrid system numerically. Parameters chosen in the simulation are found from references comprised of experimental works [24, 31-33]. We have considered AuNPs as our MNP with the following parameters,

radius $r_m = 5nm$, plasmon frequency $\epsilon_M = 8.55eV$, high plasmon frequency $\epsilon_\infty = 1.53eV$, and decay frequency $\gamma_M = 0.073$, all found from reference [33]. We consider PbS QDs with a rabi frequency $\Omega_{QD} = 50meV$ and a decay $\Gamma_{QD} = 5meV$ [31]. Both the PbS QDs and AuNP are embedded in a polymethylmethacrylate dielectric substrate. The dielectric substrate has the following parameters, permittivity $\epsilon_d = 1.96$, and permeability $\mu_d = 1$. On top of the dielectric substrate lays the SRM. The SRM in consideration is a metamaterial comprised of left and right inductors and capacitors with a decay $\gamma_s = 40$meV. Inductances and capacitances of the SRM are taken as $L_r = 8.67 \times 10^{-14}H$ and $C_r = 0.5 \times 10^{-17}F$ with $L_r/L_l = 0.01$ and $C_r/C_l = 7$ [24]. Other parameters we have considered are $g_l = -1$ and $\zeta = 0.1$ due to the parallel polarization and spherical polarization respectively. Resonance frequencies for SRM and MNP are calculated by using equations (4.7-4.15), and are ϵ_{SRM}=0.920eV and ϵ_{MNP}=0.998eV, respectively.

The PL quenching factor for the hybrid system has been calculated. PL quenching factor is plotted as a function of energy (eV) in Figure 4.2. The solid curve represents PL quenching factor in a system of QDs alone, while the dash, dot, and dash-dot curves correspond to PL quenching in a QD-MNP-SRM hybrid system. Notice the minima, this is due to the dipole-dipole interaction between the excitons from the QDs and the SPPs from MNP and SRM. Results above are consistent with recent theoretical work of Singh et al. and of experimental data of Noginov et al. who studied similar metamaterial dye doped structures [28,34].

Now we evaluate the PL quenching spectrum for the QD-MNP-SRM hybrid system. In Figure 4.3 we study the effect R_{QM} has on the QD's PL output. We have plotted PL(nW) as a function of energy (eV), in Figure 4.3. The dashed and dotted curves correspond to R_{QM}= 15nm and R_{QM}= 20nm, respectively, while $R_{QS} = R_{SM}$=10nm. Notice in the Figure 4.3 there are two sets of peaks; Figure 4.3A represents excitons-SRM interaction, while Figure 4.3B is located near the excitons-MNP interaction. Another interesting result is the difference in PL output between the two sets of peaks. Figure 4.3B has a much larger PL output compared to the Figure 4.3A. This indicates that the exciton-SRM interaction is much stronger than the

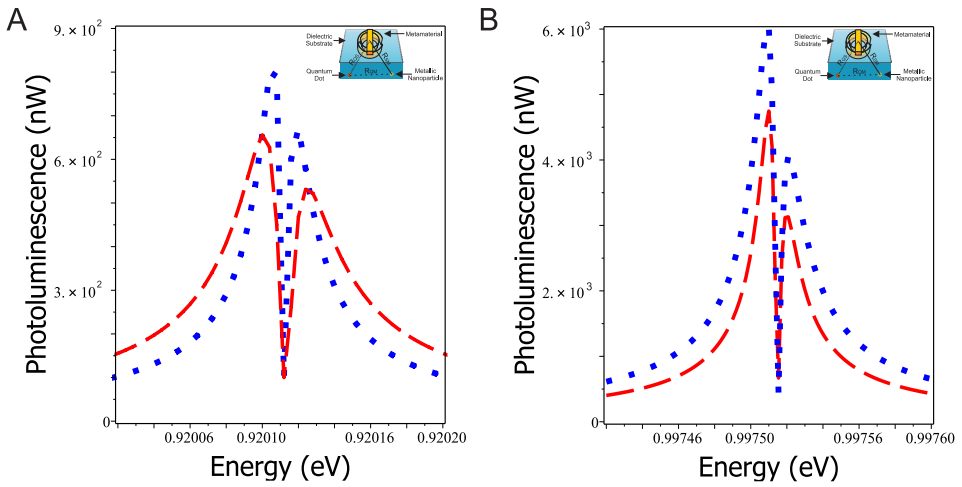

Figure 4.3: PL emission spectra of a QD-MNP-SRM system. The dashed and dotted curve corresponds to distances of $R_{QM} = 15$ and $R_{QM} = 20$, respectively, while $R_{QS} = R_{SM} = 10nm$.

exciton-MNP interaction, due to a larger nonradiative energy transfer from the QD to SRM via MNP. Further examining Figure 4.3A and Figure 4.3B, we notice as R_{QM} increases the PL output increases from the QD. This increase is due to a decrease in nonradiative decay which decreases the quenching effect. The decrease in nonradiative decay and the weaker exciton-MNP interaction is also responsible for the narrowing of the PL spectrum.

The most striking feature illustrated in these two figures is the dip in PL near the two SPP resonance frequencies. This lack of emission is caused by quantum interference in the two possible decay channels. Here, due to the SPPs from the MNP and SRM causes the transition energy between $|a\rangle \leftrightarrow |b\rangle, \epsilon_{ab}$, and $|a\rangle \leftrightarrow |c\rangle, \epsilon_{ac}$, to split into ϵ^{+}_{ab} and ϵ^{-}_{ab}, and ϵ^{+}_{ac} and ϵ^{-}_{ac}. Therefore, attempting to stimulate a PL response one will see a transparent state, because of mismatch energies. Lastly, the asymmetry is also caused by the local field.

Next, we investigate the effect R_{QS} has on the QD's PL output. In Figure 4.4 we have plotted PL(nW) as a function of energy (eV). The dashed and dotted curves correspond to R_{QS}= 15nm and R_{QS}= 20nm, respectively, while R_{QM}= R_{SM}=10nm. Similar results are found in Figures 4-4 compared to Figures 4-3. Two peaks are present and are located near ϵ_{SRM} and ϵ_{MNP}, and the narrowing of the PL spectrum increases as R_{QS} increases, seen in Figures 4-4 Insert.

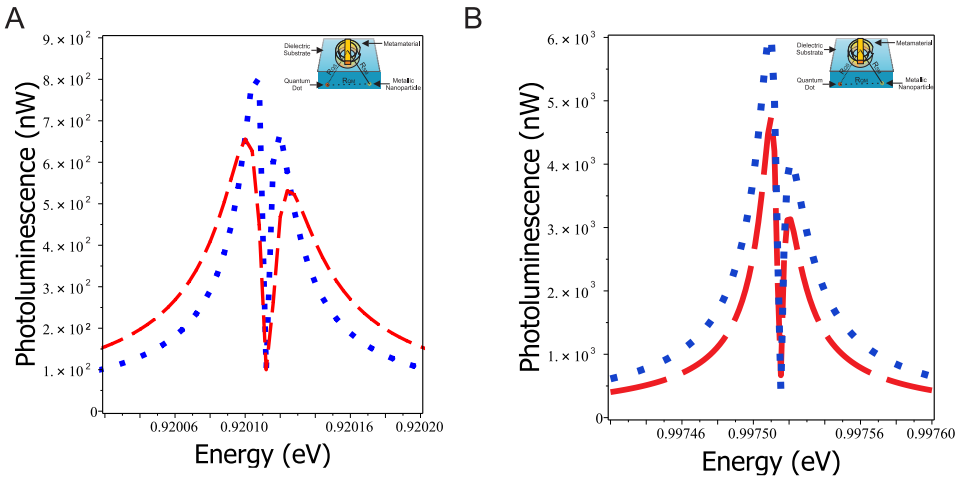

Figure 4.4: PL emission spectra of a QD-MNP-SRM system. The dashed and dotted curve corresponds to distances of $R_{QS} = 15nm$ and $R_{QS} = 20nm$, respectively, while $R_{QM} = R_{SM} = 10nm$.

Figure 4.4A and Figure 4.4B further illustrate that as R_{QS} increase the PL output increases from the QD, and the PL spectrum narrows. Again both peaks are increasing PL output due to the decreasing quenching factor because of nonradiative decay. Note, Figure 4.4B has a larger output then Figure 4.4A, because of the stronger exciton-SRM interactiong in the system. Comparing Figure 4.4 with Figure 4.3, we notice the heights to be the same. Thus suggesting that the distance has a similar affect on the system, and it is the dominate term. In Figure 4.5, we calculate in the change PL spectrum due to an increasing R_{SM}. We have plotted PL(nW) as a function of energy (eV). Dashed and dotted curves correspond to R_{QS}= R_{QS}=10nm, with R_{SM}=15nm, and R_{SM}=15nm, respectively. As in the two prior figures two peaks are located near ϵ_{SRM} and ϵ_{MNP} and as the distance changes the linewidth of the curve also alters. As R_{SM} increase the PL output increases from the QD cause by the decreasing quenching factor. Comparing Figure 4.5 with Figure 4.3 and 4.4 we notice one dramatic distance. The PL output is two orders of magnitude smaller than the previous PL outputs. This suggests that changing the distance between SRM and MNP has a negligible effect compared to changing the distance between QD to SRM and MNP. In other words, the direct fields have more of an impact than the indirect fields. The indirect fields could be considered a fine adjustment variable, while

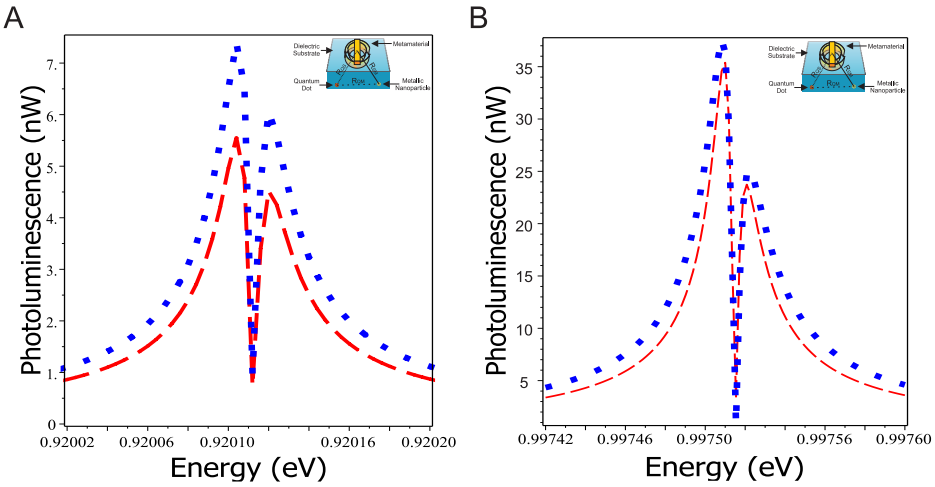

Figure 4.5: PL emission spectra of a QD-MNP-SRM system. The dashed and dotted curve corresponds to distances of $R_{SM} = 15nm$ and $R_{SM} = 2nm0$, respectively, while $R_{QM} = R_{QS} = 10nm$.

the direct fields a coarse adjustment variable. From these results variations in distance can be achieved by applying strain and stress fields, which would allow these systems to be used as sensors or switches.

4.4 Conclusions

In summary, we have studied PL quenching of doped QDs in a QD-MNP-SRM nano-hybrid system. We have used the density matrix method to develop theoretical formulation for the quenching factor and PL in our nanohybrid. To describe the QD-probe field, exciton-SRM and exciton-MNP dipole fields we used the second quantization Hamiltonian method. Following this method, we were able to calculate the expressions for power emitted. Results, showed strong PL quenching near exciton resonance frequency, and as distances in the system increase an increase in PL spectrum was noticed. Theoretical formulations of PL can be easily interchanged to calculate the PL quenching seen on the MNP or SRM. Finding from this paper can lead to new types of optoelectronic devices for nanosensing, and nanoswitching.

Bibliography

[1] Y. Li, S. Kita, P. Muoz, O. Reshef, D.I. Vulis, M. Yin, M. Lonar, and E. Mazur, Nat. Photonics 9, 738 (2015).

[2] D. Chanda, K. Shigeta, S. Gupta, T. Cain, A. Carlson, A. Mihi, A.J. Baca, G.R. Bogart, P. Braun, and J.A. Rogers, Nat. Nanotechnol. 6, 402 (2011).

[3] C.L. Cortes, W. Newman, S. Molesky, and Z. Jacob, J. Opt. 14, 063001 (2012).

[4] A. Poddubny, I. Iorsh, P. Belov, and Y. Kivshar, Nat. Photonics 7, 948 (2013).

[5] S. V Zhukovsky, T. Ozel, E. Mutlugun, N. Gaponik, A. Eychmuller, A. V Lavrinenko, H. V Demir, and S. V Gaponenko, Opt. Express 22, 18290 (2014).

[6] S.P. Rodrigues, Y. Cui, S. Lan, L. Kang, and W. Cai, Adv. Mater. 1124 (2014).

[7] W.D. Newman, C.L. Cortes, and Z. Jacob, J. Opt. Soc. Am. B-Optical Phys. 30, 766 (2013).

[8] R.D. Artuso and G.W. Bryant, Phys. Rev. B - Condens. Matter Mater. Phys. 82, (2010).

[9] E. Oh, M.-Y. Hong, D. Lee, S.-H. Nam, H.C. Yoon, and H.-S. Kim, J. Am. Chem. Soc. 127, 3270 (2005).

[10] M. Li, X. Zhou, S. Guo, and N. Wu, Biosens. Bioelectron. 43, 69 (2013).

[11] A. Samanta, Y. Zhou, S. Zou, H. Yan, Y. Liu, P. Long, and R. Spectroscopic, Nano Lett. (2014).

[12] R. Freeman, X. Liu, and I. Willner, J. Am. Chem. Soc. 133, 11597 (2011).

[13] Z. Liu, P. Yin, H. Gong, P. Li, X. Wang, and Y. He, J. Lumin. 132, 2484 (2012).

[14] M. Noh, T. Kim, H. Lee, C.K. Kim, S.W. Joo, and K. Lee, Colloids Surfaces A Physicochem. Eng. Asp. 359, 39 (2010).

[15] I.-S. Liu, H.-H. Lo, C.-T. Chien, Y.-Y. Lin, C.-W. Chen, Y.-F. Chen, W.-F. Su, and S.-C. Liou, J. Mater. Chem. 18, 675 (2008).

[16] L. Li, G. Wu, T. Hong, Z. Yin, D. Sun, E.S. Abdel-Halim, and J.J. Zhu, ACS Appl. Mater. Interfaces 6, 2858 (2014).

[17] Y. Li, Y. Hu, Y. Zhao, G. Shi, L. Deng, Y. Hou, and L. Qu, Adv. Mater. 23, 776 (2011).

[18] Y. Matsumoto, R. Kanemoto, T. Itoh, S. Nakanishi, M. Ishikawa, and V. Biju, J. Phys. Chem. C 112, 1345 (2008).

[19] X. Wu, H. Liu, J. Liu, K.N. Haley, J.A. Treadway, J.P. Larson, N. Ge, F. Peale, and M.P. Bruchez, Nat. Biotechnol. 21, 41 (2003).

[20] X. Zeng, S. Ma, J. Bao, W. Tu, and Z. Dai, Anal. Chem. 85, 11720 (2013).

[21] K.V. Sreekanth, A. De Luca, and G. Strangi, Sci. Rep. 3, 3291 (2013).

[22] H.N. Krishnamoorthy, Z. Jacob, E. Narimanov, I. Kretzschmar, and V.M. Menon, in OSA/CLEO/QELS 2010 (2010), p. JWA23.

[23] L.N. Tripathi, T. Kang, Y.-M. Bahk, S. Han, G. Choi, J. Rhie, J. Jeong, and D.-S. Kim, Opt. Express 23, 14937 (2015).

[24] K. Tanaka, E. Plum, J.Y. Ou, T. Uchino, and N.I. Zheludev, Phys. Rev. Lett. 105, 351 (2010).

[25] D. Sarid and W. Challener, Modern Introduction to Surface Plasmons: Theory, Mathematica Modeling, and Applications (Cambridge Univeristy Press, New York, 2010).

[26] E. Le Ru and P.G. Etchegoin, Principles of Surface-Enhanced Raman Spectroscopy (Elsevier Science, Philadelphia, 2008).

[27] L. Novotny and B. Hecht, Principles of Nano-Optics, 2nd Editio (Cambridge University Press, Cambridge University Press, 2006).

[28] M.R. Singh, J.D. Cox, and M. Brzozowski, J. Phys. D. Appl. Phys. 47, 085101 (2014).

[29] M.R. Singh, Advance Quantum Physics (Wiley Customs, Toronto, 2014).

[30] M.R. Singh, Electronic, Photonic, Polaritonic, and Plasmonic Materials (Wiley Customs, Toronto, 2014).

[31] I. Hemdana, M. Mahdouani, and R. Bourguiga, Phys. B Condens. Matter 407, 3313 (2012).

[32] J.R. Schaibley, a P. Burgers, G. a McCracken, D.G. Steel, a S. Bracker, D. Gammon, and L.J. Sham, Phys. Rev. B 87, 115311 (2013).

[33] P.G. Etchegoin, E.C. Le Ru, and M. Meyer, J. Chem. Phys. 125, 164705 (2006).

[34] M.A. Noginov, H. Li, Y.A. Barnakov, D. Dryden, G. Nataraj, G. Zhu, C.E. Bonner, M. Mayy, Z. Jacob, and E.E. Narimanov, Opt. Lett. 35, 1863 (2010).

[35] O.G. Calderon, M.A. Anton, and F. Carreno, Eur. Phys. J. D - At. Mol. Opt. Phys. 25, 77 (2003).

Chapter 5

Light absorbtion in quantum dots and nano-hole metamaterial structure

In the prior chapter we examined the optical properties in a system composed of quantum dots, metallic nanoparticles and a metamaterial. Photoluminescence in the quantum dots was quenched due to the interaction between excitons in the quantum dot with the surface plasmon polaritons energies of the metamaterial and metallic nanoparticles. In this chapter, we investigate the absorption spectrum of quantum dots in the vicinity of nano-hole array metamaterial. Here we study the effects different modes of surface plasmons from the metamaterial have on the quantum dots.

5.1 Introduction

There is a considerable interest in developing nanoscale plasmonic devices used for sensing by combining metamaterials with quantum dots (QDs) into hybrid nanostructures [1-10]. Metamaterials come in a variety of shapes and structures. For nanostructures to be classified as a metamaterial the unit cell must be much smaller than that of the applied interacting wave. In this chapter we consider a gold nano-hole array structure, which we will denote as NAS, as our metamaterial. Other types of structures have been experimentally studied [2-4]. Research on

metamaterial hybrid nanostructures could also lead to applications in quantum computing and communication as well as numerous applications in biophotonics and sensing.

Most of the research on nanoplasmonics has focused mainly on noble metals [11-16]. Research in noble metal hybrids is concentrated in nanophotonic applications such as integrated photonic systems [17-19], biosensing [20, 21], photovoltaic devices [22], and single photon transistors for quantum computing [23, 24]. The problem with the noble metals is that they are hardly tunable and exhibit large Ohmic losses which limit their applicability to plasmonic and optoelectronic devices. Metamaterials provide a possible solution to the task at hand. Metamaterials can allow for a much tighter confinement, small Ohmic losses and have relatively long propagation distances compared with noble metals.

In this chapter the QD-NAS are deposited on Pyrex substrate. A schematic diagram for the hybrid system is shown in Figure 5-1. Here we calculate the interaction between excitons in the QD with SPPs in NAS. It is considered that QD has three-energy levels in the V-configuration and contains two excitonic states. The interaction between excitons and SPPs is also called the dipole-dipole interaction. A probe field couples with surface plasmons of the NAS and produce SPPs. Therefore, we can consider a coupling between excitons in the QD with SPPs. Using the density matrix method we have calculated the absorption coefficient of the QD in the presence of exciton-SPPs couplings. It is found that when the first and second exciton energies of the QD are not in resonance with the SPP energies the absorption spectrum has two similar peaks in the visual range. However, when the first and second exciton energies are resonant with the SPP energies then there is an enhancement in the absorption spectrum of the two peaks. This enhancement is due to the transfer of SPP energies from the NAS to the QD. In other words, the energy transfer from the NAS to the QD can be switched ON and OFF by mismatching the resonant energies of excitons and polaritons. The mismatching of energies can be achieved by applying external pump laser or stress and strain fields. These are fascinating findings and they can be used to fabricate switches and sensors in the visible energy range.

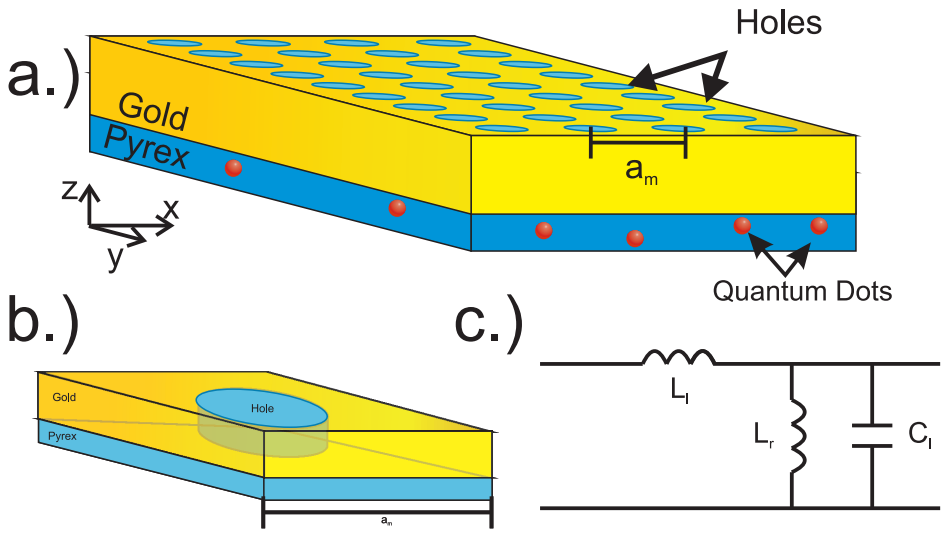

Figure 5.1: a) A schematic diagram of NAS-QD hybrid system deposited on Pyrex. b) Unit cell of the NAS is illustrated. c) An electric schematic of the SRM unit cell, composed of capacitors and inductors.

5.2 Theoretical Formalism

5.2.1 Surface plasmon polaritons in nano-hole structure

In this section we calculate the SPPs in a nano-hole array (NAS) structures. The NAS are fabricated in metallic thin film by Carson and group at Western [25]. A schematic diagram of NAS is shown in Figure 5-1. They have fabricated the nano-hole array structure in a 100-nm thick gold film on the Pyrex substrate. The nano-holes are arranged in a periodic array. The radius of these holes is in the order of 50 nm and periodicity of the lattice is in range of 360nm. This NAS can also be classified as a metamaterial due to fact that it is a newly engineered periodic structure with unit cell size much smaller than wavelength of light we are using [25]. In the rest of the paper we can exchange the nomenclature between the NAS with metamaterial.

Recently calculations of dielectric constant of the NAS structure using the transmission line theory and Bloch's theorem was calculated[25]. The transmission line theory is widely used to calculate band structures of metamaterials which are periodic structures [26, 27]. Nano-holes are arranged periodically in a cubic lattice structure. Each nano-hole can also be described

as a nano-hole rod. The radius of these rods is taken as r, and the length of nano-hole rod is considered to be l. The periodicity of the structure is taken as a_p. The nano-hole can by characterized by a self-inductance L_r. The inductance and capacitance per length l of the transmission line are L_l and C_l, resulting in the unit cell diagram seen in Figure 5-1C. The expression of the dielectric constant is found as [25]

$$\epsilon_s = \left[\frac{2c}{a_p \omega} sin^{-1} \left(\frac{\omega}{\sqrt{2}\omega_m} \sqrt{1 - \frac{\omega_p^2}{\omega^2 + i\gamma_m \omega}} \right) \right]^2 . \tag{5.1}$$

Here $\omega_p = \hbar / \sqrt{L_r C_r}$ and $\omega_m = 0.1\omega_p$

The metamaterial is deposited on a Pyrex substrate. The dielectric constant of Pyrex is denoted as ϵ_d and it is found as $\epsilon_d = 6.4$ experimentally. SPPs exists at the interface of the NAS and Pyrex. Using the transfer matrix method, the SPPs dispersion is found in reference [25] and it is written as

$$k_\beta = G_1(\omega) \pm G_2(\omega) \tag{5.2}$$

$$G_1(\omega) = \left(\frac{\frac{n\pi}{a_p} F_d^4}{F_s^4 - F_d^4} \right) \qquad G2(\omega) = \sqrt{G_1(\omega) - \left(\frac{n\pi}{a_p} \right)^2 \frac{F_d^4}{F_d^4 - F_s^4} - \frac{F_d^2 F_s^2}{F_d^2 + F_s^2}}$$

where n is Brillouin's number and $F_d = \omega \sqrt{\epsilon_d}/(\hbar c)$ and $F_s = \sqrt{\epsilon_s}$.

We have plotted the SPP dispersion relation of NAS where the solid curve corresponds to n=0 and the dashed curve corresponds to n=1. The dispersion relation for our system is plotted in Figure 5-2 as a function of energy and wave vector. The solid curve corresponds to the first SPP mode (n=0) and the dashed curve represents the second SPP mode (n=1). The SPP frequencies can be calculated from the figure when the wave vector k_β reaches infinity. They were computed to be $\hbar\omega_{SP1} = 1.90eV$and $\hbar\omega_{SP2} = 2.30eV$ for n=0 and n=1, respectively. Note that calculation of the SPP values from the polarizability method agree well with experiments by Carson group [25].

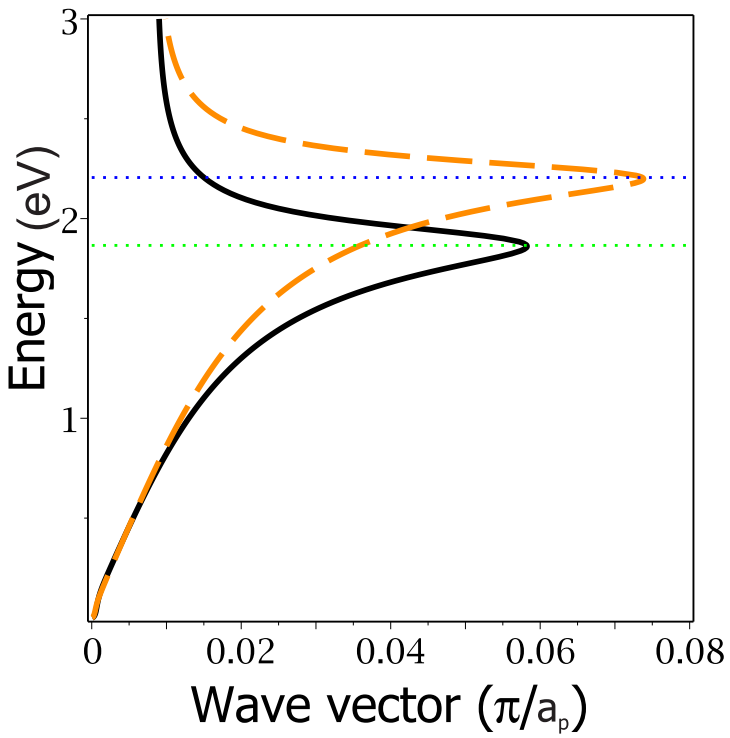

Figure 5.2: Surface plasmon polariton dispersion relation of the nano-hole metamaterial structure. Solid curve corresponds to n=0 while the dashed curve represents n=1. Other parameters include a_p = 360nm and r = 50nm.

5.2.2 Coupling of Quantum emitter and nano-hole structure

In the above section we have found that the NAS structure contains two SPP modes located at $\hbar\omega_{SP1} = 1.90eV$ and $\hbar\omega_{SP2} = 2.30eV$. We want observe the effect of these two SPP modes on the absorption coefficient of the quantum dot. They are deposited near the interface between the NAS and Pyrex slabs. Hence the QD can see the electric field produced by the two SPP modes near the interface. We consider that QDs have two excitonic states located near the SPP modes $\omega_{SP1}$and ω_{SP2}. Two excitons in a QD can be obtained by considering that the QD that has three discrete electronic levels which are denoted as $|a\rangle$, $|b\rangle$ and $|c\rangle$ where $|a\rangle$ is the ground state whereas $|b\rangle$ and $|c\rangle$ are excited states. A schematic diagram of the QD is shown in Figure. 5-2. The transition frequencies of two excitons for transitions $|a\rangle \leftrightarrow |b\rangle$ and $|a\rangle \leftrightarrow |c\rangle$ are denoted as ω_{ab} and ω_{ac}, respectively. We consider that ω_{ab} and ω_{ac} are resonant with $\omega_1^{sp}$and

ω_2^{sp}, respectively.

We apply a probe field with amplitude E_P and frequency ω to monitor the absorption for the transitions $|a\rangle \leftrightarrow |b\rangle$ and $|a\rangle \leftrightarrow |c\rangle$. The probe field induces a dipole moment P_{QD} in the QD due to the transition $|a\rangle \leftrightarrow |b\rangle$ and $|a\rangle \leftrightarrow |c\rangle$. The dipole moment in turn produces an electric field E_{QD} nearby.

$$E_{QD}=\frac{g_l P_{QD}}{4\pi\epsilon_{an}R^3} \tag{5.3}$$

where R is the center-to-center distance between the QD and the NAS and $\epsilon_{an} = (2Re(\epsilon_s) + \epsilon_a)/3\epsilon_a$. Here ϵ_s is the dielectric constant of the QD and ϵ_a is the dielectric constant of the medium surrounding the NAS system. The constant g_l is called the polarization parameter and it has values $g_l = -1$ and $g_l = 2$ for $P_{QD} \shortparallel E_p$ and $P_{QD} \perp E_p$, respectively, found in previous chapters. The polarization of the QD is calculated by using the density matrix method in the later section. It is calculated as follows in terms of the density matrix elements [28]

$$P_{QD} = (\mu_{ab}\rho_{ab} + \mu_{ac}\rho_{ac}) + c.c. \tag{5.4}$$

where μ_{ij} and ρ_{ij} are the dipole moment and density matrix element, respectively for the transition $|i\rangle \leftrightarrow |j\rangle$ and c.c represent complex conjugate, similarly found in the previous chapters. Here ρ_{ij} and ρ_{ji} satisfy the condition $\rho_{ij}^* = \rho_{ji}$.

There are two electric fields that are falling on the NAS structure. One is the probe field and another is the induced QD electric field. These two fields excite the two SPPs modes as discussed in the previous section. The electric fields produced one SPP modes at the QD is calculated as [29, 30]

$$E_{SP} = \frac{g\,(E_P + E_{QD})}{4\pi\epsilon_{an}}\alpha_{SP} \tag{5.5}$$

Here α_{SP} represents the polarizability of the SPPs. It is seen below and is similar to equation (4.15)

$$\alpha_{SP} = \frac{A_n\epsilon_{an}^2 V_N}{g}e^{-k_{dx}x} \tag{5.6}$$

where V_n is the volume of the NAS, and $k_{dx} = \sqrt{k_\beta - F_d}$. Constant A_n is calculated using the normalization condition as

$$A_n = \frac{\mu_s Re(k_{dx}) - \mu_d Re(k_{mx})}{\mu_s Re(k_{dx}) + \mu_d Re(k_{mx})} \tag{5.7}$$

here $k_{mx} = \sqrt{k_\beta - F_m}$

We have shown the that the SPP electric field has two modes ω_{SP1} and ω_{SP2}. Note that the electric field produced by the NAS depends on the polarizability, α_{SP}, which is a complex quantity. Polarizability, α_{SP}, of the NAS has a huge value at the SPP frequencies $\omega = \omega_{SP1}$ and $\omega = \omega_{SP2}$ for other value of ω the polarizability is negligible which is seen in reference [25]. Hence, in the rest of the calculations we will evaluate the polarizability at the ω_{SP1} and ω_{SP2} resonance frequencies. In so, we denote $\alpha_{SP} = \alpha_{SP1}$ for $\omega = \omega_{SP1}$ and $\alpha_{SP} = \alpha_{SP2}$ for $\omega = \omega_{SP2}$. Thus the total electric field produced by the NAS can be written as

$$E_{NAS} = E_{SP1} + E_{SP2} \tag{5.8}$$

where

$$E_{SP1} = E_P + E_{QD}^{SP1} \tag{5.9}$$

$$E_{SP2} = E_P + E_{QD}^{SP2} \tag{5.10}$$

Note that E_{NAS} consists of the two electric fields E_{SP1} and E_{SP2} which correspond to ω_{SP1} and ω_{SP12}, respectively.

Now we consider that the resonance frequency ω_{ab} of transition $|a\rangle \leftrightarrow |b\rangle$ is in resonance with the SPP resonance frequency ω_{SP1} i.e. $\omega_{ab} = \omega_{SP1}$ while the resonance frequency ω_{ac} of transition $|a\rangle \leftrightarrow |c\rangle$ is in resonance with the SPP resonance frequency ω_{SP2} i.e. $\omega_{ab} = \omega_{SP2}$. In this situation the expressions for the ω_{SP1} and ω_{SP2} fields after substituting the expression of

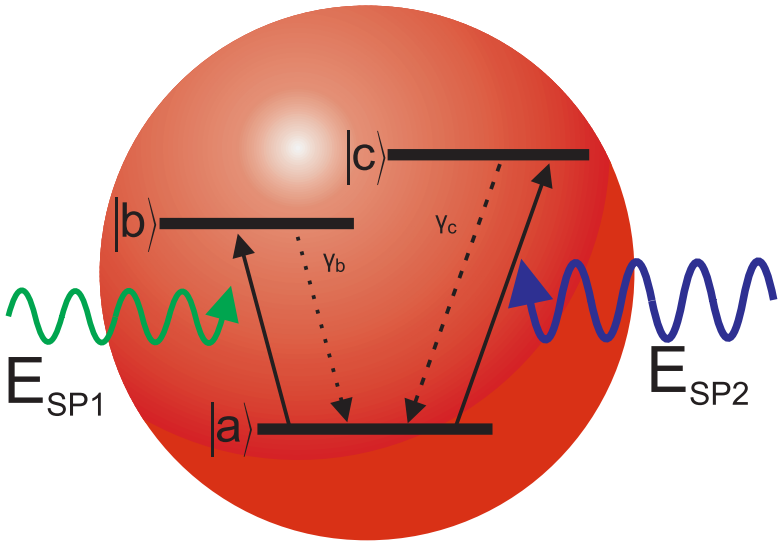

Figure 5.3: A schematic diagram of a QD with three energy levels in a V-configuration. Level |a⟩ indicates the ground level while levels |b⟩ and |c⟩ corresponds to two excited states. Metamaterial's SPP (when n=0) couples with transition |a⟩ - |b⟩ of the QD while metamaterial's SPP (when n=1) couples with transition |a⟩ - |c⟩.

E_{QD} from equation (5.3) into equations (5.9-5.10) reduce to

$$E_{SP1} = E_P + \frac{g_l \mu_{ab} \rho_{ab}}{4\pi\epsilon_{an} R^3} \alpha_{SP1} E_P + cc \tag{5.11}$$

$$E_{SP2} = E_P + \frac{g_l \mu_{ac} \rho_{ac}}{4\pi\epsilon_{an} R^3} \alpha_{SP2} E_P + cc \tag{5.12}$$

The first and second terms in the above expression are due to the probe field and the QD dipole field, respectively

5.2.3 Exciton-SPP interactions

In this section we calculate the interaction of the QD with the electric fields of the NAS and the external probe field. A schematic diagram of this interaction is shown in Figure 5-3. The Hamiltonian of the exciton in the QD can be written as

$$H_{EX} = \hbar\omega_a\sigma_{aa} + \hbar\omega_b\sigma_{aa} + \hbar\omega_c\sigma_{cc} \tag{17}$$

where $\sigma_{ii} = |i\rangle\langle i|$ with i=a,b,c.

The induced dipole in QD interacts with electric fields falling on the QD. The external probe field E_P interacts with the QD via excitons transitions $|a\rangle \leftrightarrow |b\rangle$ and $|a\rangle \leftrightarrow |c\rangle$. We have also found that the ω_{SP1} electric field E_{SP1} produced by the NAS when n=0, is acting on the exciton transition $|a\rangle \leftrightarrow |b\rangle$ and the ω_{SP2} electric field E_{SP2} produced by the NAS when n=1, is acting on the exciton transition $|a\rangle \leftrightarrow |c\rangle$. Therefore, the total electric field E_{ab} acting on the exciton $|a\rangle \leftrightarrow |b\rangle$ (i.e. ε_{ab}-exciton) and the total electric field acting E_{ac} on the exciton $|a\rangle \leftrightarrow |c\rangle$ (i.e. ε_{ac}-exciton) are written as

$$E_{ab} = \frac{E_P}{\epsilon_{ad}} + \frac{E_{SP1}}{\epsilon_{ad}} \tag{5.13}$$

$$E_{ac} = \frac{E_P}{\epsilon_{ad}} + \frac{E_{SP2}}{\epsilon_{ad}} \tag{5.14}$$

where ϵ_{ad} is the effective constant of the QD in its surroundings.

Putting the value of E_{SP1} and E_{SP2} from equations (5.11-5.12) into the above equation we get

$$E_{ab} = \frac{E_P}{\epsilon_{ad}} + \frac{g_l}{4\pi\epsilon_{ad}\epsilon_{an}R^3}\alpha_{SP1}\frac{E_P}{\epsilon_{ad}} + \frac{g_l^2\mu_{ab}^2\rho_{ab}}{(4\pi)^2\epsilon_{an}^2R^6}\alpha_{SP1}\frac{E_P}{\epsilon_{ad}} + cc \tag{5.15}$$

$$E_{ac} = \frac{E_P}{\epsilon_{ad}} + \frac{g_l}{4\pi\epsilon_{ad}\epsilon_{an}R^3}\alpha_{SP2}\frac{E_P}{\epsilon_{ad}} + \frac{g_l^2\mu_{ab}^2\rho_{ab}}{(4\pi)^2\epsilon_{an}^2R^6}\alpha_{SP2}\frac{E_P}{\epsilon_{ad}} + cc \tag{5.16}$$

where the first term is the probe field contribution and the second and third terms are the contributions from the NAS dipole fields.

The dipole of the QD interacts with the electric field E_{ab} and E_{ac}. The interaction Hamilto-

nian of the QD is expressed in the dipole and the rotating wave approximation as

$$H_{int} = -\mu_{ab}E_{ab}\sigma_{ba} - \mu_{ac}E_{ac}\sigma_{ca} + h.c. \tag{5.17}$$

where h.c. stands for the Hermitian conjugate and $\sigma_{ba} = |b\rangle\langle a|$ and $\sigma_{ca} = |c\rangle\langle a|$ are the exciton creation operators. Putting the expressions for E_{ab} and E_{ac} from equations (5.15-5.16) into the above expression we get

$$H_{int} = \left(\Omega_p + \Pi_{SP1} + \Lambda_{SP1}\right)\sigma_{ba} + \left(\Omega_p + \Pi_{SP2} + \Lambda_{SP2}\right)\sigma_{ca} + h.c. \tag{5.18}$$

where

$$\Pi_{SP1} = \frac{g\alpha_{SP1}}{4\pi\epsilon_{an}\epsilon_{ad}}\Omega_P, \qquad \Pi_{SP1} = \frac{g\alpha_{SP2}}{4\pi\epsilon_{an}\epsilon_{an}}\Omega_P \tag{5.19}$$

$$\Lambda_{SP1} = \frac{g_l^2\mu_{ab}^2\rho_{ab}\alpha_{SP1}}{(4\pi)^2\epsilon_{an}^2\epsilon_{ad}R^6}\Omega_P, \quad \Lambda_{SP2} = \frac{g_l^2\mu_{ac}^2\rho_{ac}\alpha_{SP2}}{(4\pi)^2\epsilon_{an}^2\epsilon_{ad}R^6}\Omega_P \tag{5.20}$$

where Ω_p is Rabi frequency of the probe laser field E_P.

The H_{int} Hamiltonian given in equation (5.21) can be expressed in the interaction representation as

$$H_{int} = H_{EX-F} + H_{EX-SP1} + H_{EX-SP2} \tag{5.21}$$

where

$$\begin{aligned} H_{QD-F} &= -\hbar\Omega\sigma_{ba}e^{-i\left(\omega_p-\omega_{ab}\right)t} - \hbar\Omega\sigma_{ca}e^{-i\left(\omega_p-\omega_{ac}\right)t} + h.c. \\ H_{EX-SP1} &= \left(\Pi_{SP1} + \Lambda_{SP1}\right)\sigma_{ba}e^{-i\left(\omega_p-\omega_{ab}\right)t} + h.c. \\ H_{EX-SP2} &= \left(\Pi_{SP1} + \Lambda_{SP1}\right)\sigma_{ca}e^{-i\left(\omega_p-\omega_{ac}\right)t} + h.c. \end{aligned} \tag{5.22}$$

The first term H_{QD-F} in equation (5.21) is the interaction between the exciton and the external probe field E_p. The second term H_{EX-SP1} represents the interaction between the excitons in QD and SPP mode 1. Similarly, the third term H_{EX-SP2} represents the interaction between the

excitons in QD and SPP mode 2.

Note that two interaction terms (i.e. H_{EX-SP1} and H_{EX-SP2}) have two terms Π and Λ. The first term is due to the interaction of the QD with the dipole electric field from the NAS induced by the probe field. Therefore, we refer to this as the *direct QD-NAS* term. The second contribution is due to the interaction of the QD with a dipole field from NAS that arises when the external fields polarize the QD, which in turn polarize NAS. In other words, this contribution is the self-interaction of the QD, as it depends on the polarization of the QD. For this reason, this term is called the *self-induced QD-NAS* term.

5.2.4 Absorption coefficient and Density matrix method

We use the density matrix method to evaluate the absorption coefficient due to exciton transitions $|a\rangle \leftrightarrow |b\rangle$ and $|a\rangle \leftrightarrow |c\rangle$. Using equations. (5.17) and (5.23) for the Hamiltonian of the system and the master equation for the density matrix we obtained the following equations of motion for the QD density matrix elements

$$\frac{d\rho_{cc}}{dt} = -2\gamma_c\rho_{cc} - i\left(\Omega_p + \Pi_{SP2} + \Lambda_{SP2}\right)\rho_{ac} - i\left(\Omega_p + \Pi_{SP2} + \Lambda_{SP2}\right)^*\rho_{ca} \tag{5.23}$$

$$\frac{d\rho_{ca}}{dt} = -(\frac{\gamma_c}{2} + i\Delta_{ac})\rho_{ca} - i\left(\Omega_p + \Pi_{SP2} + \Lambda_{SP2}\right)(\rho_{cc} - \rho_{aa}) - i\left(\Omega_p + \Pi_{SP1} + \Lambda_{SP1}\right)\rho_{cb} \tag{5.24}$$

$$\frac{d\rho_{bb}}{dt} = -2\gamma_b\rho_{bb} - i\left(\Omega_p + \Pi_{SP1} + \Lambda_{SP1}\right)\rho_{ab} - i\left(\Omega_p + \Pi_{SP1} + \Lambda_{SP1}\right)^*\rho_{ba} \tag{5.25}$$

$$\frac{d\rho_{ba}}{dt} = -(\frac{\gamma_b}{2} + i\Delta_{ab})\rho_{ba} - i\left(\Omega_p + \Pi_{SP1} + \Lambda_{SP1}\right)(\rho_{bb} - \rho_{aa}) - i\left(\Omega_p + \Pi_{SP2} + \Lambda_{SP2}\right)\rho_{bc} \tag{5.26}$$

$$\frac{d\rho_{cb}}{dt} = -[\frac{(\gamma_c + \gamma_b)}{2} + i(\Delta_{ac} - \Delta_{ab})]\rho_{cb} + i\left(\Omega_p + \Pi_{SP2} + \Lambda_{SP2}\right)\rho_{ab} - i\left(\Omega_p + \Pi_{SP1} + \Lambda_{SP1}\right)^*\rho_{ca} \tag{5.27}$$

Here $\Delta_{ab} = \omega_{ab} - \omega$ and $\Delta_{ac} = \omega_{ac} - \omega$ are called the probe field detunings. Physical quantities γ_b and γ_c are the decay rates of the levels $|b\rangle$ and $|c\rangle$, respectively.

The absorption coefficient due to absorption of a photon for the transitions $|a\rangle \leftrightarrow |b\rangle$ and

$|a\rangle \leftrightarrow |c\rangle$ is calculated in the literature [30] and it is written as

$$\alpha = \alpha_0 \,\mathrm{Im}\,(\rho_{ab} + \rho_{ac}) \tag{26}$$
$$\alpha_0 = \frac{\mu_{ab}\omega_p}{\hbar c E_p},$$

where $\mu_{ab} = \mu_{ac}$ is considered. Matrix elements ρ_{ab} and ρ_{ac} appearing in the above expression will be evaluated numerically in the next section.

5.3 Results and Discussion

We consider a metamaterial composed of a gold nano-hole array structure. The thickness of the gold film is 100nm, with a nano-holes radus of 60nm and a lattice constant of a_p =400nm. Other parameters of the metamaterial are C_l= 2.50aF, L_r= 36.3fH, L_l= 26.3fH and γ_N= 0.4eV. These parameters are consistent with reference [25]. The SPP resonance (energies) frequencies for the NAS are calculated from Figure 5-2 and are found as ε_{sp1} =1.90eV and ε_{sp2} =2.30eV. The dielectric constant and dipole moments of the QD are taken as $\epsilon_d = 12$ and $\mu_{12} = \mu_{13} = 0.1$ $e \times$ nm, respectively, while the decay rates for the QD are taken as $\gamma_b = \gamma_c$=0.005eV. The radius of the QD is taken to be 3nm. These parameters are comparable to those commonly found in the literature for QDs [2-4]. The transition energies in the QD are considered to lie near the two polaritons energies as $\varepsilon_{ac} = \varepsilon_{sp2}$ and $\varepsilon_{ab} = \varepsilon_{sp1}$. These energy range are found in the QD made from HgTe[31].

Now we investigate the absorption coefficient of the QD using equation (5.26). The density matrix element ρ_{ab} and $\rho_{\mathbf{ac}}$ which appears in equation (5.26) are obtained by solving equations (5.23-5.27) numerically using a seventh-eighth order continuous Runge–Kutta method provided by the software package Maple.

First we study the effect of the exciton-SPPs and the results are plotted in Figure 5-4A and 5-4B for R=15nm. In Figure 5-4A the absorption coefficient is plotted as a function of energy (eV). Here we have focused our investigation to the visible range. The solid curve corresponds

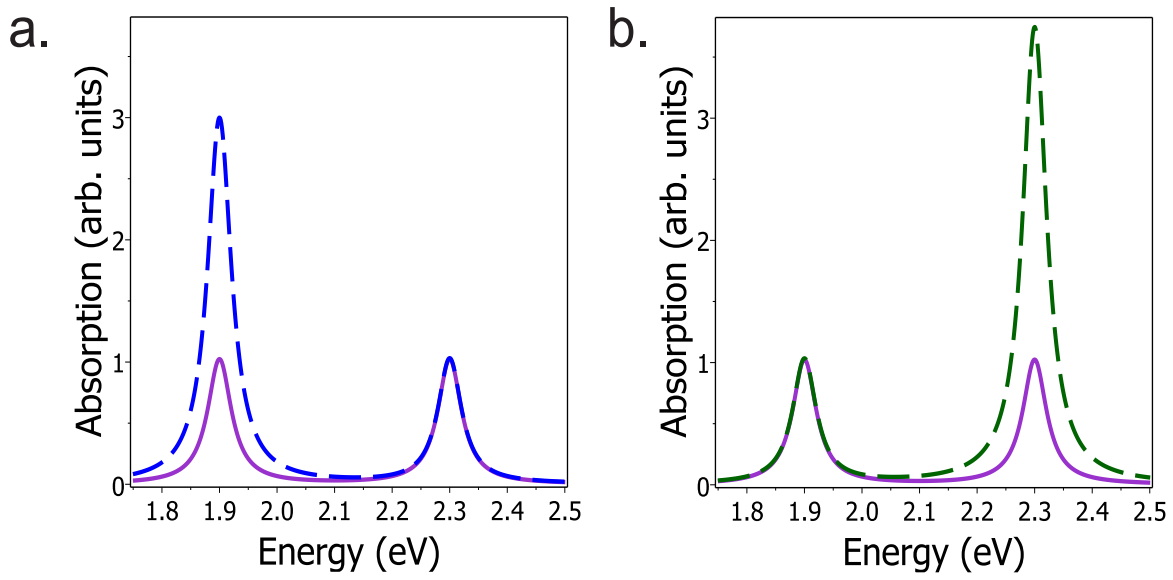

Figure 5.4: Plot of the absorption coefficient of the QD as a function of energy for (a) when the SPP of the first mode (n=0) resonants with the QD and (b) when the SPP from the second mode (n=1) resonants with the QD. Solid curves correspond to the energies where both modes of SPPs are not resonant with the QD.

to the case when exciton energies for transitions $|a\rangle \leftrightarrow |c\rangle$ and $|a\rangle \leftrightarrow |b\rangle$ are not resonant with polariton energies (i.e. $\varepsilon_{ab} \neq \varepsilon_{sp}$ and $\varepsilon_{ac} \neq \varepsilon_{pp}$). While the dash curve represents the case when the exciton transition $|a\rangle \leftrightarrow |b\rangle$ is resonant with first mode SPP energies (i.e. n=0) and exciton transition $|a\rangle \leftrightarrow |c\rangle$ is not resonant with the second SPP energy (i.e. n=1). Note that the solid curve has two peaks where the left peak is related to transition $|a\rangle \leftrightarrow |b\rangle$ and the right peak is related to transition $|a\rangle \leftrightarrow |c\rangle$. In this case the heights of both peaks are the same. This is because the coupling between QD and the MGF is negligible since the exciton and polariton energies are not in resonant.

Note that in the dashed curve in Figure 5-4a the left peak is higher than that of the right peak. This is because the coupling between ε_{ab}-exciton and the first SPP mode is strong since the exciton and polariton energies are in resonance. However, there is no coupling between ε_{ac}-exciton and since the second SPP energy mode is not in resonance. In this case the first SPP mode's energy is transferred to the QD and the absorption peak is enhanced. The energy transfer between QD and NAS can be controlled by mismatching the resonance condition be-

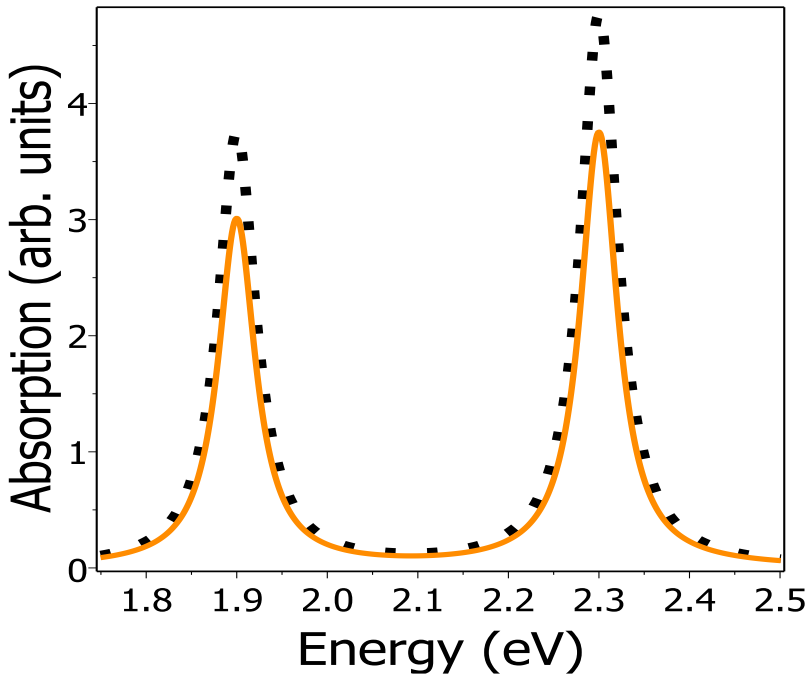

Figure 5.5: Plot of the absorption coefficient of the QD as a function of energy for when both modes of the SPPs resonant with the QD. The solid curve corresponds to when R, the center-to-center distance between components, is R = 15nm while the dashed curve corresponds to R= 13.5nm.

tween QD exciton energy and SPP energy. One of the methods to achieve the mismatch is by applying high intense ultrafast control laser field which will modify the energies of the exciton and polaritons. This is an interesting finding which can be used to fabricate the switches and sensors from the QD-NAS system in the visible range.

In Figure 5-4B we investigate the effect of the second mode exciton-SPP coupling on the absorption coefficient. The absorption coefficient is plotted as a function of energy (eV). The solid curve corresponds to the case when excitons and polaritons energies are not resonant (i.e. $\varepsilon_{ab} \neq \varepsilon_{sp1}, \varepsilon_{ac} \neq \varepsilon_{sp2}$) while the dash curve represents the case when exciton transition $|a\rangle \leftrightarrow |c\rangle$ is resonant with the second SPP energy mode and there is no coupling between ε_{ab}-exciton and the first SPP mode. In this case in the right peak, the dashed curve has a higher value than that of the left peak. This is because the coupling between ε_{ac}-exciton and the second SPP mode is strong since their energies are resonant. Here the SPP energy is transferred to the QD and the

right absorption peak is enhanced. Another thing to point out is that the scale of Figure 5-4B is larger than that of Figure 5-4A. This means that the energy transfer from the second SPP mode to the QD is larger than that of the first SPP mode.

Now we investigate the effect both exciton-SPP coupling modes while varying distance between the QD and NAS in Figure 5-5. The absorption coefficient is plotted as a function of energy (eV) in Figure 5-5. The solid and dotted curves are plotted for R=15nm and R=13.5nm, respectively when both exciton and polariton energies are in resonance. There are two enhanced peaks where the left peaks correspond to the first mode and the right represents the second mode. The height of the right is higher than that of the left peak. This means energy transfer from NAS's second exciton-SPP coupling mode is larger than that of the first exciton-SPP coupling mode. It is also found that the heights of both peaks increase as the R decreases. This means the energy transfer increases between two systems when they are close to each other.

Finally, we study the time development of the absorption coefficient with and without exciton coupling. Determining when the steady state occurs is important in calculating the density matrix solutions. We have plotted the normalized absorption coefficient (α/α_0) against normalized time ($\tau = \gamma_b t/2$) in Figure 5-6A for the ϵ=2.27eV. Here the solid and dashed curves correspond to the presence and absence of exciton coupling, respectively. Note that the absorption oscillates with time for both cases. Number of oscillations is the same for the cases but the steady state is reached at a later time in the presence of the coupling. The height of the absorption amplitude is larger with the coupling than without the coupling. This is because there is an energy transfer from the NAS to the QD. The oscillation in the absorptions are related to the Rabi oscillations. This point has been made more clear by plotting the population of excited states ($\rho_{bb} + \rho_{cc}$) with the coupling (solid curve) and without the coupling (dashed curve) in Figure 5-6B. The oscillations in the population are nothing but the Rabi oscillations. Note that the population of the excited state oscillates with time and finally reaches the steady-state after $\tau > 7$.

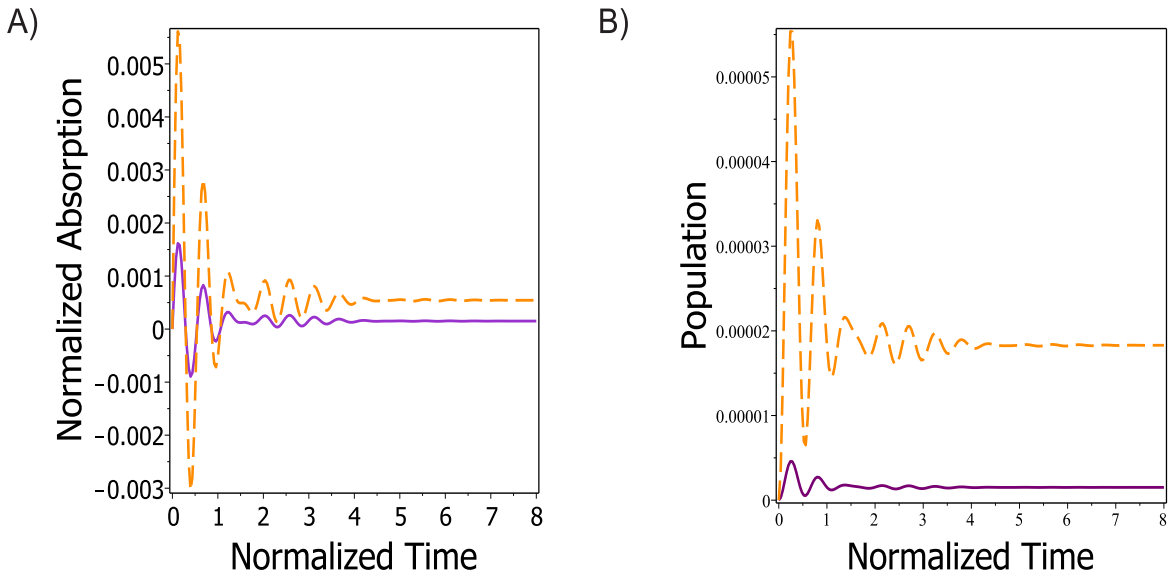

Figure 5.6: a) Plot of the normalized absorption coefficient (α/α_0) as a function of normalized time, $\tau = \gamma_b 2/2$. b) Plot of the population as a function of normalized time, $\tau = \gamma_b 2/2$. The dashed curves and solid curves correspond to when the system is in resonance and non-resonance, respectively. Other parameters include R=15nm, $\epsilon = 2.27eV$

5.4 Conclusion

We have investigated the interaction between excitons in the QD with SPPs in NAS by calculating the absorption coefficient of the QD. The QD-NAS nanocomposite is deposited on the dielectric substrate, Pyrex. Using the density matrix method, we have calculated the absorption coefficient of the QD in the presence of exciton-SPPs coupling. It is found that when the exciton energies of the QD are not in resonance with the SPP energies the absorption spectrum has two peaks in the visible range and both peaks have the same height. However, in the resonant condition, heights of two absorption peaks are higher compared to that of the non-resonance condition. This is due to the transfer of polarition energies from the NAS to the QD. In other words, the energy transfer from the NAS to the QD can be switched ON and OFF by mismatching the resonant energies of excitons and polaritons. The mismatching of energies can be achieved by applying an external pump laser or stress and strain fields. These are interesting findings and they can be used to fabricate switches and sensors in the THz energy range.

Bibliography

[1] N. Liu, T. Weiss, M. Mesch, L. Langguth, U. Eigenthaler, M. Hirscher, C. S??nnichsen, and H. Giessen, Nano Lett. 10, 1103 (2010).

[2] Y. Wang, T. Sun, T. Paudel, Y. Zhang, Z. Ren, and K. Kempa, Nano Lett. 12, 440 (2012).

[3] K.L. Young, M.B. Ross, M.G. Blaber, M. Rycenga, M.R. Jones, C. Zhang, A.J. Senesi, B. Lee, G.C. Schatz, and C.A. Mirkin, Adv. Mater. 26, 653 (2014).

[4] L.N. Tripathi, T. Kang, Y.-M. Bahk, S. Han, G. Choi, J. Rhie, J. Jeong, and D.-S. Kim, Opt. Express 23, 14937 (2015).

[5] Z. Fei, G.O. Andreev, W. Bao, L.M. Zhang, A. S. McLeod, C. Wang, M.K. Stewart, Z. Zhao, G. Dominguez, M. Thiemens, M.M. Fogler, M.J. Tauber, A.H. Castro-Neto, C.N. Lau, F. Keilmann, and D.N. Basov, Nano Lett. 11, 4701 (2011).

[6] M.R. Singh, J.D. Cox, and M. Brzozowski, J. Phys. D. Appl. Phys. 47, 085101 (2014).

[7] T. Chen, S. Li, and H. Sun, Sensors 12, 2742 (2012).

[8] Z.G. Dong, H. Liu, J.X. Cao, T. Li, S.M. Wang, S.N. Zhu, and X. Zhang, Appl. Phys. Lett. 97, (2010).

[9] I.A.I. Al-Naib, C. Jansen, and M. Koch, Appl. Phys. Lett. 93, (2008).

[10] J.F. OHara, R. Singh, I. Brener, E. Smirnova, J. Han, A.J. Taylor, and W. Zhang, Opt. Express 16, 1786 (2008).

[11] M. Achermann, J. Phys. Chem. Lett. 1, 2837 (2010).

[12] R.D. Artuso and G.W. Bryant, Phys. Rev. B - Condens. Matter Mater. Phys. 82, (2010).

[13] S.M. Sadeghi, L. Deng, X. Li, and W.-P. Huang, Nanotechnology 20, 365401 (2009).

[14] M.-T. Cheng, S.-D. Liu, H.-J. Zhou, Z.-H. Hao, and Q.-Q. Wang, Opt. Lett. 32, 2125 (2007).

[15] M. Durach, A. Rusina, V.I. Klimov, and M.I. Stockman, New J. Phys. 10, (2008).

[16] J.M. Luther, P.K. Jain, T. Ewers, and A.P. Alivisatos, Nat. Mater. 10, 361 (2011).

[17] D.K. Gramotnev and S.I. Bozhevolnyi, Nat. Photonics 4, 83 (2010).

[18] L. Novotny and N. van Hulst, Nat. Photonics 5, 83 (2011).

[19] J.A. Schuller, E.S. Barnard, W. Cai, Y.C. Jun, J.S. White, and M.L. Brongersma, Nat. Mater. 9, 193 (2010).

[20] a V Kabashin, P. Evans, S. Pastkovsky, W. Hendren, G. a Wurtz, R. Atkinson, R. Pollard, V. a Podolskiy, and a V Zayats, Nat. Mater. 8, 867 (2009).

[21] H.X. Xu, E.J. Bjerneld, M. Kll, and L. Brjesson, Phys. Rev. Lett. 83, 4357 (1999).

[22] H.A. Atwater and A. Polman, Nat. Mater. 9, 205 (2010).

[23] D.E. Chang, A.S. Srensen, E.A. Demler, and M.D. Lukin, Nat. Phys. 3, 807 (2007).

[24] A. Gonzalez-Tudela, D. Martin-Cano, E. Moreno, L. Martin-Moreno, C. Tejedor, and F.J. Garcia-Vidal, Phys. Rev. Lett. 106, (2011).

[25] M.R. Singh, M. Najiminaini, S. Balakrishnan, and J.J.L. Carson, J. Appl. Phys. 117, 184302 (2015).

[26] C. Caloz and T. Itoh, Electromagnetic Metamaterials: Transmission Line Theory and Microwave Applications: The Engineering Approach (2005).

[27] L. Solymar and E. Shamonina, Waves in Metamaterials (Oxford University Press, London, 2009).

[28] M.R. Singh, Advance Quantum Physics (Wiley Customs, Toronto, 2014).

[29] D. Sarid and W. Challener, Modern Introduction to Surface Plasmons: Theory, Mathematica Modeling, and Applications (Cambridge Univeristy Press, New York, 2010).

[30] M.R. Singh, Electronic, Photonic, Polaritonic, and Plasmonic Materials (Wiley Customs, Toronto, 2014).

Chapter 6

Concluding Remarks

In this thesis, plasmonics and nanophotonics were studied in a variety of polaritonic nano-hybrids. The nano-hybrids discussed in this thesis include quantum dot-metallic nanoparticle/graphene nanocomposites, quantum dot-metamaterial nanocomposites and quantum dot-metallic nanoparticles/metamaterial nanocomposites. Numerical calculations were performed these three systems. Results presented the new nano-hybrids with novel optical properties that exceeded the capabilities of the individual components. It is anticipated that these discoveries presented in this thesis can be used to motivate future theoretical and experimental work on nano-hybrids made with quantum dots, graphene, metallic nanoparticles, and metamaterials.

In chapter 3, photoluminescence quenching theory was developed for a quantum emitter, metallic nanoparticle and graphene hybrid system. Using many body theory called the quantum density matrix method and Maxwell's equations in the quasi-static approximation we are able to calculate the dipole-dipole interactions between the nanocomposites. Considering the quantum Golden rule, we calculate the radiative and nonradiative decay processes in the presence of dipole-dipole interaction. Results show that photoluminescence quenching in our hybrids occurs not only due the direct nonradiative energy transfer but also through the indirect nonradiative energy transfer process. It is found that the indirect nonradiative process in depends on the distance between the nanocomponents. With our theory we are able to compare our

theory with photoluminescence quenching in similar systems, and a good agreement is found between the two. These are fascinating results which can be used to fabricate nanoswitches and nanosenors for medical applications.

In chapter 4, we studied photoluminescence quenching in a nano-hybrid composed of quantum dots, metallic nanoparticles and split-ring metamaterials, incorporating external and local fields. The density matrix method was used to develop theory for photoluminescence quenching in metamaterial hybrid structure. Using the second quantization Hamiltonian method we are able to evaluate expression for the power emitted of the quantum dot, with three interacting dipole fields. When the dipole-dipole interaction fields resonant with the excitons in the quantum dots a strong photoluminescence quenching was observed. As distances between components decreases, photoluminescence quenching increased. Theoretical formulations of photoluminescence can be easily interchanged to calculate the photoluminescence quenching seen on the metallic nanoparticles or split-ring metamaterials. Finding from this chapter can lead to new types of optoelectronic devices for nanosensing, and nanoswitching.

Lastly, we have investigated quantum dot absorption between the interactions of surface plasmon polaritons from a gold nano-hole array structure with the excitons of a quantum dot. We classify the gold nano-hole array structure as a metamaterial, deposited on Pyrex. We have numerically calculated absorption spectrum by solving the density matrix method. Our results show when resonant conditions are met, absorption peaks are enhanced compared to non-resonant conditions. Energy is transfer from the metamaterial to the quantum dot. The energy transfer from the metamaterial to the quantum dot can be switched ON and OFF by mismatching the resonant energies of excitons and polaritons. These are interesting findings and they can be used fabricate switches and sensors in the visible energy range.

Chapter 7

Future Work

In the prior chapter we summarized the thesis as a whole. Finally, we discuss further possible work that can be implemented.

In Chapter 3, we developed a theory which studied energy transfer in hybrid nanosystem made with quantum emitters, metallc nanoparticles and graphene. We considered the metallic nanoparticles and the graphene to have surface plasmon polaritons which arise from the coupling of surface plasmons with a probe field. We solve classically the dispersion relation for the surface plasmon polaritons. These polaritons interact with excitons in the quantum emitters via exciton-SPP interaction, where energy is exchanged. The second quantized formulation and the quantum density matrix method were used to calculate the photoluminescence. With this core based theory, our next possible step in this chapter would be to develop a full quantum theory approach. In the chapter we used the classical-quantum approach were the dispersion relation of surface plasmon polaritons was done classically and incorporated into the second quantized formulation and the quantum density matrix method. Hence, evolving the classical dispersion relations to quantum relations can be a future step.

In Chapter 4, photoluminescence quenching was studied for quantum dots doped in metallic nanoparticle and split-ring metamaterial hybrid system. With this theory we included local fields. Results showed photoluminescence was quenched as distances reduced between seg-

ments. This occurs only when exciton transition energies are resonant with surface plasmon polaritons energies. Similarly to Chapter 3, a full quantum theory can be established. Other future possibility would be to further explore the effect local fields has on photoluminescence quenching.

In the final content chapter, light-matter interaction in quantum dots and metamaterial was investigated. We use the density matrix method to solve absorption coefficient of the quantum dot in the presence of the exciton-SPP coupling. Again we have taken the classical approach when solving the dispersion relation of the surface plasmon polaritons, and a full quantum theory could be derived. Lastly another future path would be to study the phonon contribution to the system. It is known that phonon can produce phonon polaritons [1]. Thus, the inclusion of these phonon polaritons might provide some interesting results.

Bibliography

[1] N. Ocelic, and R. Hillenbrand, Nat. Mat 3, 606 (2004)

Curriculum Vitae

Name:	Marek Brzozowski
Post-Secondary Education and Degrees:	The University of Western Ontario London, Ontario, Canada 2008 - 2013 B.Sc. Specialization in Physics and Major in Medical Cell Biology
Related Work Experience:	Teaching Assistant The University of Western Ontario 2013 - 2015

Publications:

Singh M, **Brzozowski M**, and Racknor C, 2015 Induced transparencies in metamaterial waveguides doped with quantum dots J. Phys. D 48 145301

Singh M, Cox J, and **Brzozowski M**, 2014 Photoluminescence and spontaneous emission enhancement in metamaterial heterostructures, J. Phys. D 47 085101.

Communicated or in Preparation:

Brzozowski M, and Singh M, 2015 The effect of surface plasmon polaritons modes on the energy absorption in quantum dots and nano-hole metamaterials structures.

Brzozowski M, and Singh M, 2015 Photoluminescence quenching theory in metamaterial, quantum dots and metallic nanoparticles hybrid systems, J. Phys. D

Brzozowski M, and Singh M, 2015 Photoluminescence quenching, metallic nanoparticle and graphene hybrid nanomaterials, J. Opt. Soci. America

Singh M, Fainberg B, **Brzozowski M**, and Aptar B, 2015 The effect of phonon-plasmon and surface plasmon polaritons on the energy absorption in quantum dots and graphene nanocomposite deposited on polar crystals, Phys. Rev. B